Validation of edge turbulence codes in a magnetic X-point scenario in TORPEX

D. Galassi[1], C. Theiler[1], T. Body[2], F. Manke[1], P. Micheletti[1],
J. Omotani[3], M. Wiesenberger[4], M. Baquero-Ruiz[1], I. Furno[1], M. Giacomin[1],
E. Laribi[5], F. Militello[3], P. Ricci[1], A. Stegmeir[2], P. Tamain[5], H. Bufferand[5],
G. Ciraolo[5], H. De Oliveira[1], A. Fasoli [1], V. Naulin[4], S. L. Newton[3], N. Offeddu[1],
D. S. Oliveira[1], E. Serre[6], N. Vianello[7]

December 12, 2021

[1] *École Polytechnique Fédérale de Lausanne (EPFL), Swiss Plasma Center (SPC), CH-1015 Lausanne, Switzerland*
[2] *Max Planck Institut für Plasmaphysik, Boltzmannstr. 2, 85748 Garching, Germany*
[3] *United Kingdom Atomic Energy Authority, Culham Centre for Fusion Energy, Culham Science Centre, Abingdon, Oxon, OX14 3DB, UK*
[4] *Department of Physics, Technical University of Denmark, DK-2800 Kgs. Lyngby, Denmark*
[5] *IRFM, CEA Cadarache, F-13108 St. Paul-lez-Durance, France*
[6] *Aix-Marseille Université, CNRS, Centrale Marseille, M2P2, Marseille, France*
[7] *Consorzio RFX, Corso Stati Uniti 4, 35127, Padova, Italy*
e-mail address: davide.galassi@epfl.ch

Abstract

Transport processes around the magnetic X-point of tokamaks, such as turbulence and mean-field drifts, are scarcely understood. The assessment of the capability of turbulence codes to quantitatively reproduce these dynamics has been hampered by limitations in computational power and available experimental data. In this paper, we present a rigorous validation of full-scale simulations of a newly developed X-point scenario in the basic toroidal plasma device TORPEX, performed with the four state-of-the-art codes FELTOR, GBS, GRILLIX and STORM. High-resolution Langmuir probe array measurements of various time-averaged and fluctuating quantities and across the entire cross-section of TORPEX show that this X-point scenario features the key ingredients of X-point dynamics, such as small-scale fluctuations as well as background drifts. The codes are able to qualitatively reproduce some characteristics of the time-averaged fields, such as the ion saturation current profiles at mid-height, the plasma up-down asymmetry and the blob trajectories. A quantitative agreement is found for the background $E \times B$ velocity pattern, while the fluctuation levels are generally underestimated by typically factors of 2 or more, thus background fluxes are found to dominate over turbulent ones in simulations. The sensitivity of the simulation results on the plasma collisionality and on the position of the sources are tested in GBS, showing a mild effect on the overall quantitative agreement with the experiment. Overall, this validation reveals the challenges to reproduce the plasma dynamics near an X-point, and provides a clear path to a quantitative, and computationally relatively inexpensive assessment of future developments in turbulence codes.

1 Introduction

One of the major challenges in magnetic fusion research consists in confining a burning plasma core without damaging the surrounding vacuum vessel. In tokamaks, due to an imperfect magnetic confinement of the core plasma, heat is constantly expelled into the Scrape-Off Layer (SOL), where a large part of the exhaust power is deposited on a relatively narrow layer on dedicated target plates. If unmitigated, the resulting peak target heat fluxes predicted for a reactor exceed engineering limits by an order of magnitude [1, 2, 3, 4]. The introduction of a poloidal field null or X-point in the tokamak boundary, which diverts the SOL magnetic field lines away from the core plasma to spatially separated target plates, is a key element to address this challenge. Such a divertor geometry offers well known benefits in comparison to a limited configuration [5]. Divertor geometries are more efficient in screening the core plasma from impurities and recycling neutrals generated at the plasma-wall interface, allowing detached regimes with strongly reduced contact between the SOL plasma and the target plates. They provide improved pumping capabilities of the particle exhaust, and facilitate the access to high-confinement regimes [6]. Moreover, they provide additional volume for volumetric power losses, and result in longer connection lengths in the SOL, allowing an enhanced cross-field transport, thus a spreading of the heat flux over a larger area.

At the same time, however, the presence of an X-point results in a considerable increase in the complexity of the highly non-linear SOL dynamics, governed by an interplay of turbulence, background drifts, sources and sinks. A complicated flow pattern associated mainly with $E \times B$ drifts is observed in two-dimensional (2D) transport codes [7] and in three-dimensional (3D) turbulence codes [8, 9]. In the H-mode favorable field direction, for instance, these drifts transport plasma particles from the outer divertor SOL into the Private-Flux Region (PFR) and further towards the inner divertor, causing large differences in the plasma parameters at the inner and outer targets. These background drifts co-exist and non-linearly interact with complex turbulence dynamics. Theory and experiments suggest that coherent turbulent structures called “filaments”or “blobs”, elongated along the field lines, become strongly squeezed and tilted around the X-point, due to the strong flux expansion and magnetic shear in this region, until they disconnect from the midplane [10, 11, 12]. This picture is consistent with a quiescent region in the divertor near SOL, inferred from visible imaging [13] and X-point/divertor probes [14], and the observation of blobs independent from those at the outboard midplane in the outer divertor leg close to the separatrix and in the private flux region both in experiments [15] and in simulations [16].

The most widely used tools to simulate these complex phenomena around the X-point are nowadays 3D fluid turbulence codes, even if different approaches, such as gyro-kinetic codes for the edge plasma (e.g. [17, 18]) are also rapidly developing. Turbulence codes have greatly improved, in the last years, the understanding of important phenomena occurring in the edge plasma. Scaling laws for the characteristic heat flux width at the target or the pressure decay length at the midplane (e.g. [19, 20, 21]) have been derived with 3D fluid turbulence simulations and compared with theoretical models. Ultimately, however, in order to develop full predictive capabilities, these codes need to undergo a thorough validation with experimental data. Initially, validation exercises focused on simple magnetic configurations [22, 23], while more recently they have been extended to larger experiments, as TCV (Tokamak à Configuration Variable [24]), in limiter configuration [25]. Multi-code validations of seeded blobs had been performed against TORPEX [26] and MAST [27] experiments. A multi-code validation of nonlinear flux-driven simulations against an ISTTOK poloidally limited plasma had also been carried out [28].

In this work, we extend the previous code validation efforts with the aim to assess the maturity of today's numerical tools to treat the X-point region. Our objective is to test the physical models implemented in the codes in their entirety, so their ability to describe at the same time large-scale and small-scale flows, background drifts, outflows at the boundaries, and ultimately their ability to reproduce the global system behavior in time and space. For this purpose, a dedicated X-point scenario is developed in the TORoidal Plasma EXperiment (TORPEX) [29, 30, 31]. TORPEX is a basic plasma device operated at the EPFL, Switzerland. Due to relatively low plasma densities and temperatures, TORPEX allows for full diagnostic access. In addition, thanks to a relatively large ion sound Larmor radius with respect to typical tokamaks, full-size simulations of TORPEX plasmas are readily accessible. An extensive experimental dataset, including measurements of both time-averaged and fluctuating quantities in a wide 2D spatial domain, is built. Despite TORPEX not being a device with reactor-relevant plasma parameters, the X-point scenario developed in this work features key ingredients of tokamak X-point physics, such as the interaction of background drifts and curvature-induced turbulent transport around the X-point, and it is thus suitable as benchmark for the validation of the models implemented in turbulence codes.

The simulations of this scenario are performed with the state-of-the-art, 3D, flux-driven turbulence codes FELTOR [32], GBS [21], GRILLIX [33] and STORM [34], which are able to describe the nonlinear interaction of profiles, turbulence, and flows with realistic X-point geometry and the presence of closed and open field lines [32, 9, 35, 36, 37]. First, a qualitative comparison between simulations and experiments is carried out. Then, a rigorous validation is performed with the procedure described in Ricci et al, 2011 [23], developed following a similar approach to the one proposed by Terry et al, 2008 [38]. The results of the validation show that, in particular, the background $E \times B$ velocity pattern around the X-point is well predicted by the codes, while the present simulations cannot reproduce, within the experimental errorbars, most of the fluctuation properties, or the 2D distribution of the fields in the poloidal section. As a consequence of the low fluctuation level predicted in simulations, the background $E \times B$ fluxes are the dominant transport mechanisms with respect to turbulent fluxes.

This paper is organized as follows. In Section 2 we describe the new TORPEX X-point scenario and discuss the experimental results. In Section 3 we present the setup of the simulations. In Section 4 we compare experimental results with TORPEX experiments, and we quantify the agreement of the comparison. In Section 5 we discuss a sensitivity scan of collisionality and particle source position performed with GBS, and we present the conclusions in Section 6. A detailed description of the codes used in this work is presented in Appendix A.

2 TORPEX X-point scenario

2.1 Experimental setup

The TORPEX device is composed of a toroidal stainless-steel vacuum vessel of major radius $R_0 = 1$ m and minor radius of 0.2 m, and is operated at a toroidal magnetic field on axis B_φ^0 of typically 76 mT. For a visual overview of the device, see Figure 1 in [31]. In this work, no current is induced in the plasma. Molecular hydrogen was injected in the vacuum chamber at the rate of 1 scm^{-3}/min and room temperature, and ionization was obtained by injection of microwaves in the electron cyclotron frequency range [39]. This resulted in plasma parameters of the order of $n_e \sim 10^{16}$ m^{-3} and $T_e \sim 5$ eV, and in ionization fractions of the order of 1%. Highly reproducible plasma discharges can be sustained for several minutes, although we limited the diagnostics acquisition time to approximately 2 s.

Turbulence characteristics were determined in the bulk region of the vessel with the HEXTIP-U (HEXagonal Turbulence Imaging Probe - Upgrade) system [40, 41], consisting of two Langmuir-probe arrays installed at toroidally opposite locations in TORPEX. The two arrays, dubbed HEXTIP1 and HEXTIP2 in what follows, cover the entire poloidal cross section in a hexagonal pattern with a grid constant of 3.5 cm, and an estimated collecting area of the tips $A_{HXT} = 16.2$ mm^2. In this work, the HEXTIP-U acquired data for a period of ~ 1 s per discharge, at a 250 kHz acquisition frequency. Cross-talk among neighboring probe tips was evaluated to be negligible [41]. We also measured time-averaged fields by means of SLP (Slow Langmuir Probes)[42]. SLP is a radially-movable vertical array of 8 Langmuir probes spaced by 1.8 cm, each with a collecting area $A_{SLP} = 18.9$ mm^2. The vertical position of the first tip array is fixed at the midplane ($Z = 0$), while the probe array can point upwards or downwards in order to measure at $Z \geq 0$ or $Z \leq 0$, respectively. In this work, the SLP radial position was moved by 1 cm from discharge to discharge from $R - R_0 = -12$ cm to $R - R_0 = 9$ cm, and it was operated with a 335 Hz triangular voltage sweep and a 250 kHz acquisition frequency. For each measurement point, this allows to infer the electron temperature T_e from the current-voltage (IV) characteristic curve. From the same curve, we evaluated the floating potential V_f, that, combined with the T_e measurement, gives the plasma potential ϕ via the sheath potential drop model:

$$\phi = V_f + \Lambda T_e \ , \tag{2.1}$$

where we estimate $\Lambda = 3.1$ for TORPEX. The ion saturation current density J_{sat} is simply derived dividing the current by the probe collecting area, and the electron density is obtained as:

$$n = 2\frac{J_{sat}}{ec_s} \ , \tag{2.2}$$

where the factor 2 accounts for the ion-accelerating effect in the pre-sheath forming around the probes in the bulk plasma.

2.2 The new X-point scenario

A new TORPEX magnetic field scenario was specifically designed for this work. Its key functionalities are to guarantee a good diagnostic coverage around the X-point region, to have characteristics similar to tokamaks in the vicinity of the X-point, and to comply with the numerical limitations given by the turbulence codes. Given these constraints, an X-point is created using only coils outside the vessel, contrarily to previous work [43], where an in-vessel coil was energized. This choice was driven by the necessity to have a small flux expansion between different points on the same flux surface, in order to limit the range of spatial scales that must be accounted for in turbulence codes. The resulting magnetic configuration is a simple, up-down symmetric shape without closed flux surfaces, featuring an X-point on the midplane of TORPEX. The flux surface including the X-point, from now on called “separatrix”, separates four sectors of open field lines, as shown in Figure 1. The magnetic field lines are the result of an analytic computation based on the current flowing in each coil, and not of a magnetic plasma equilibrium reconstruction.

As shown in Figure 1, the X-point is located at $R - R_0 = 1.8$ cm. An uncertainty on the radial position of the X-point of ± 0.6 cm was evaluated by means of a Hall probe, taking into account uncertainties in the vessel position.

The toroidal field at the major radius R_0 was set for this experiment to $B_\varphi^0 = 76$ mT, in counter-clockwise direction when TORPEX is observed from above. As it will be explained in Section 2.5, this toroidal field value leads to a particle source almost completely localized in the High-Field Side (HFS) sector ($R - R_0 < 0$). The ratio of the poloidal over the toroidal field at 1 cm from the X-point is $B_\theta/B_\varphi \sim 10^{-3}$, a value comparable to a TCV discharge with plasma current $I_p \sim 100$ kA, at the same position. The value of the magnetic shear is also of the same order as in a low-current tokamak shot. The connection length diverges going from the vessel to the X-point, with characteristic values of ~ 50 m at $R - R_0 = -10$ cm, corresponding to approximately 8 toroidal turns. The incidence angle of the field lines at the vessel wall is approximately 0.5° for strike points at the HFS and 1.2° at the Low-Field Side (LFS).

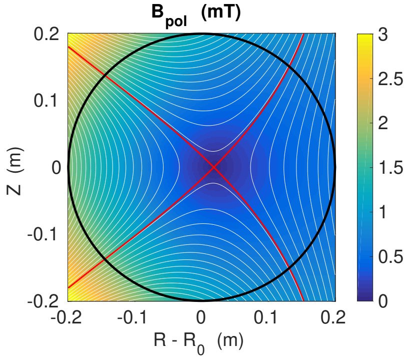

Figure 1: Poloidal cross section of TORPEX (the symmetry axis of the torus is located at the left) showing the poloidal magnetic field structure in the new X-point scenario. The black thick line represents the TORPEX vessel. White lines are iso-contours of the poloidal flux function. The separatrix is plotted in red.

2.3 Optimization of the scenario

An optimization of the experimental reference scenario in TORPEX was carried out through the tuning of several operational parameters. Several values of the toroidal field were explored, in the range of 72 mT to 78 mT. Because of the proportionality between the Electron Cyclotron (EC) frequency and B_φ^0, the particle source moves towards the LFS with larger values of the toroidal field. The value of 76 mT was chosen as reference, since lower toroidal fields gave very HFS-localized plasmas, while higher values would have caused the source to be strongly overlapped with the X-point, resulting in a more difficult interpretation of its effects on turbulence. Three values of injected microwave power, 300 W, 500 W and 700 W, were also tested. While the plasma density was found to increase with input power, as expected, the plasma underwent an outward radial shift due to the shift of the Upper Hybrid (UH) resonance layer. Besides this shift, the spatial distribution of the time-averaged density, as well as the density statistical moments, were not found to change substantially. A power of 300 W was chosen as reference.

A scan in the poloidal field magnitude was also performed. The poloidal field is given by two pairs of vertically symmetric coils, where a different value of current is injected in each pair. The measured value of the current injected in the coils has fluctuations with amplitude of ±2% of the nominal value. These fluctuations can cause a vertical displacement of the X-point of the order of 1 cm, which we do not expect to significantly impact the experimental measurements. The impact of these X-point displacements on the flux expansion along flux surfaces is negligible. In the following we characterize the magnitude of the poloidal field by the nominal current value in a given poloidal field coil I_p^c. On one hand, a high poloidal field magnitude, for a fixed toroidal field of 76 mT, leads to a high magnetic shear in the vicinity of the X-point, comparable to tokamak values. On the other hand, a high number of detected blobs is also desirable, in order to have sufficient statistics to study their generation and motion characteristics. A Conditional Average Sampling (CAS) ([44, 45]) is performed on the ion saturation current density J_{sat} collected by HEXTIP-U for each discharge in the poloidal field scan. An event is defined as a blob if at a fixed triggering position, one has $J_{sat} - \langle J_{sat}\rangle_t > 3\ std(J_{sat})$, where $\langle\cdot\rangle_t$ defines the time-average. Around each event, we define a symmetric time-window of 400 µs. For each time-step within the window, a separate average is performed across all windows, in order to reconstruct the typical blob dynamics.

I_p^c (A)	Number of detected blobs
75	100
150	32
225	34
300	16
450	2
525	4
600	0

Table 1: Number of detected blobs as a function of the current in the poloidal field coils in a time interval of 60 ms of TORPEX X-point discharges.

As visible in Table 1, the average number of blobs detected in this manner during a fixed time window decreases with increasing poloidal field. The scenario with $I_p^c = 225$ A was selected, as it features a high number of blobs, and a ratio of poloidal to toroidal field that is comparable to a tokamak in the vicinity of the X-point.

2.4 Results in the reference scenario

We performed a total of 44 discharges (selected from numbers #72760 to #72809) using the reference scenario (described in Section 2.3), which allowed us to achieve a good spatial resolution with the SLP. At the same time, HEXTIP1 was operated in ion saturation current mode (see Figure 2) while HEXTIP2 was in floating potential mode.

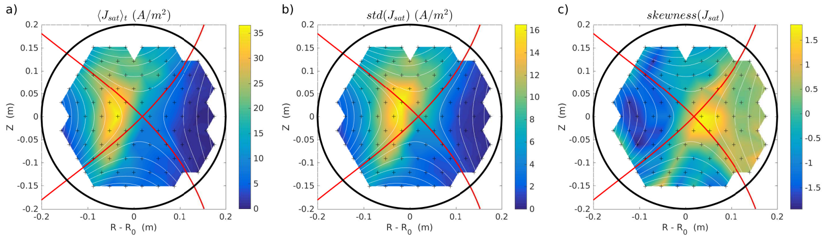

Figure 2: Ion saturation current density statistical moments measured by HEXTIP1, averaged over the shot database. The black crosses represent the position of the probe tips. a) Time average of the ion saturation current. b) Standard deviation. c) Skewness.

We notice from Figure 2a that the average ion saturation current density, whose spatial distribution can be used as a proxy for that of plasma density, has a rather strong up-down asymmetry, unlike most of the previous experiments on TORPEX (e.g. [46, 26]). The HFS sector is filled with plasma due to the source being located there. In addition, high saturation currents are measured in the top sector, in contrast with the bottom one. This suggests an asymmetry in transport mechanisms. The J_{sat} fluctuation amplitude is generally stronger where J_{sat} is stronger, with a small displacement of the maximum to the top and the LFS with respect to the J_{sat} peak. The fluctuation skewness is negative in the HFS sector and positive in the LFS one, with a peak in the vicinity of the X-point. This suggests that turbulent structures are generated in the HFS or top sectors, then move radially outwards, with large events propagating through the low-density region. This feature was already observed in TORPEX scenarios with vertical poloidal field [30], although in those cases the blob behavior was homogeneous in the vertical direction.

A series of discharges with the same poloidal field as in the reference scenario, but reversed toroidal field, was operated, acquiring data both with HEXTIP-U and SLP (shots #73035 − #73046). As expected, considering that the magnetic configuration is up-down symmetric, the resulting J_{sat}, floating potential (V_f) and electron temperature (T_e) profiles were up-down flipped with respect to the reference scenario. This excludes a possible impact on plasma behavior of non-symmetric elements, such as the in-vessel coil, placed near the top of the vessel at $R = R_0$, $Z = 17.5$ cm during the experiments described here, or the positioning of the microwave source at the bottom of TORPEX.

The CAS technique, applied to the reference series of discharges, shows that the blobs are typically born in the HFS sector, in the region where the density is highest, as shown in Figure 3a. The turbulent structures propagate then upwards and towards the LFS, approximately following the direction of the separatrix. The conditionally averaged blob propagates with a velocity of the order of 1 km/s, similarly to previous studies in different magnetic configurations [43, 47]. The blob is associated to a dipolar structure in electric potential, which is observed on the floating potential (Figure 3b). The electric field associated to this dipolar structure, of the order of 0.1 kV/m, is comparable to the background, time-averaged electric field, which we can infer from SLP measurements of plasma potential. This is shown in Figure 3c, where the steady-state $E \times B$ velocity pattern is also represented. One can notice that, at least in the top part of the device, the background $E \times B$ drift velocity reaches its largest magnitude in the proximity of the separatrix, and its direction is approximately aligned to the separatrix. The plasma potential spatial distribution is clearly determined by the electron temperature, whose measurements are shown in Figure 3d.

Several trigger locations have been tested for the CAS, especially in the LFS region with high skewness, in order to understand if different blob propagation patterns are present. This test shows that the fluctuations measured at far LFS locations are the result of the spreading of relatively large blobs propagating through the X-point or the upper branch of the separatrix. From this analysis, a clear pattern for the generation and propagation of blobs in this scenario emerges. After being generated in a high-density region, blobs propagate upwards and towards the LFS, through the vicinity of the X-point, then progressively lose amplitude before reaching the TORPEX vessel. The propagation of these blobs is caused by both background $E \times B$ drift, and by the local, self-induced dipolar structures of the potential. These components contribute to a comparable extent to the blob propagation, confirming the importance of a multi-scale analysis of the problem.

In order to gain insight into the turbulence dynamics in the parallel direction, we evaluated the correlation of turbulent structures by operating in ion saturation current mode both HEXTIP1 and HEXTIP2. In most of the poloidal section, the field lines pitch angle is small, and plasma fluctuations appear to be toroidally aligned, showing very similar time traces at two tips at identical poloidal location in the two arrays. This observation indicates a "resistive" interchange instability, which was extensively described in [48]. Only in regions far from the X-point the toroidal alignment is lost, and we observe the field alignment typical of an "ideal" ballooning instability. This is due to the fact that the poloidal field is stronger in this region, and turbulent structures cannot toroidally self-connect anymore. This is in quantitative agreement with modelling predictions and previous TORPEX

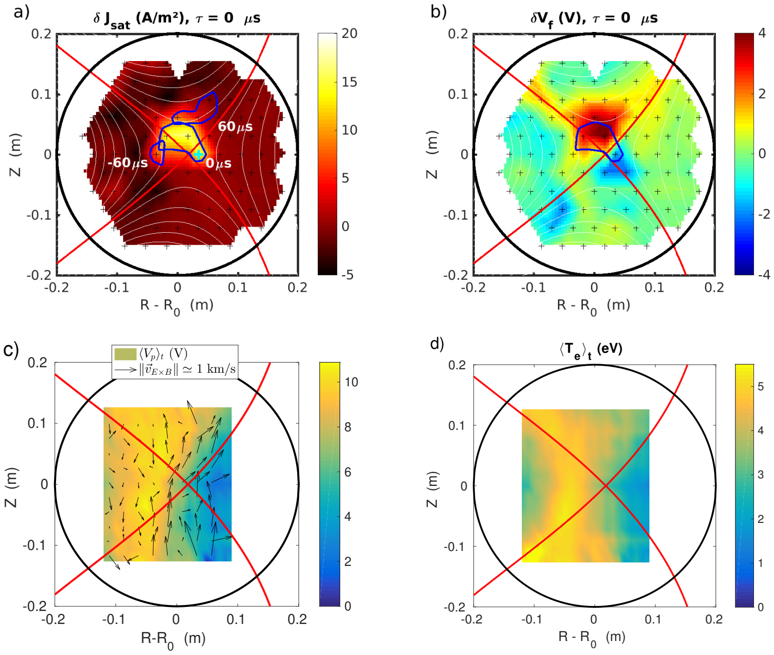

Figure 3: a) Blob propagation dynamics obtained from Conditional Average Sampling. The color plot shows the averaged J_{sat} fluctuation at the triggering time $\tau = 0$. In blue, the contours correspondent to $0.6max(J_{sat}(\tau))$, for $\tau = -60$ µs, $\tau = 0$ µs and $\tau = +60$ µs. The triggering location is indicated by the cyan cross. b) Conditionally averaged V_f fluctuations at the triggering time. In blue, the corresponding J_{sat} contour. c) Average plasma potential measured by SLP. Black arrows indicate the corresponding $E \times B$ velocity field. The arrow length is proportional to the speed, which can be compared to the 1 km/s of the arrow in the legend. d) Electron temperature measured by SLP.

experiments [48], which found a transition from ideal to resistive interchange instability when the field line connecting two vessel points makes a number of toroidal turns $N > 7$. In our case, at the midplane, this condition is fulfilled everywhere except for $R - R_0 < -12$ cm and $R - R_0 > 14.5$ cm, where we actually observe field aligned-structures. In these peripheral regions, in fact, the maximum correlation between the ion saturation current signal in HEXTIP1 and HEXTIP2 is found at the probes which are field aligned, and not at the ones which are toroidally aligned.

2.5 Source determination by power modulation

Dedicated experiments were carried out to determine the profiles of the particle source, needed as an input for the simulations. Most of the deposited energy of the injected microwaves is absorbed by the plasma at the EC and, more importantly, at the UH resonance layers [49]. While the EC layer position depends only on the norm of the total field (to a good approximation equal to the toroidal field), and can thus be determined *a priori*, the UH layer position and shape depend on plasma density through the relation:

$$R_{UH} = R_{EC}\sqrt{\left(1 - \frac{ne^2}{f_{RF}^2 4\pi^2 \epsilon_0 m_e}\right)^{-1}}, \tag{2.3}$$

where R_{EC} is the radial position of the EC resonance layer, n is the plasma density, and $f_{RF} = 2.4$ GHz is the frequency of the injected microwaves. The method described in [39] was adopted for the determination of the particle source. The microwave power was modulated using a square wave with minimum injected power $P_{min} = 300$ W (our baseline value) and maximum power $P_{max} = 1200$ W, with duty cycle of 10% and frequency of 250 Hz. We measured with HEXTIP1 the average perturbation in the ion saturation current density ΔJ_{sat} with respect to the low-power phase. The measurement was taken after the nominal beginning of each high-power phase, at $\Delta t = 17$ µs, in order to avoid the influence of transport phenomena. Then, the measurements in all the power cycles were averaged. Under the assumption that the spatial distribution of the particle source is similar to that of the increment in measured saturation current ($S_n(R, Z) \propto \Delta J_{sat}$), and that the perturbations of the background plasma are negligible ($\Delta J_{sat} \ll \langle J_{sat}\rangle_t$), we obtain the source spatial distribution illustrated in Figure 4.

In order to numerically implement the sources in the codes, they were fitted with the function f_S:

$$f_S = \begin{cases} \exp\left[-\left(\frac{R-R_S}{a}\right)^2 - \left(\frac{Z-Z_S}{b}\right)^2\right] & \text{if } R > R_S \\ \frac{1}{2}\exp\left[-\left(\frac{R-R_S}{a}\right)^2 + c\,(R-R_S)\,(Z-Z_S) - \left(\frac{Z-Z_S}{b}\right)^2\right] & \\ +\frac{1}{2}\exp\left[-\left(\frac{R-R_S}{a}\right)^2 - c\,(R-R_S)\,(Z-Z_S) - \left(\frac{Z-Z_S}{b}\right)^2\right] & \text{if } R \leq R_S \end{cases}, \tag{2.4}$$

where $R_S = 0.98$ m and $Z_S = 0.02$ m, and parameters a, b, c have been optimized to fit the source function. The fit function f_S, represented by contour lines in Figure 4, is up-down symmetric, although shifted downwards in the vertical direction with respect to the midplane by 2 cm. We further assume that the electron energy source has the same spatial distribution as the particle source. The ion power source is neglected, since for typical TORPEX plasmas $T_i \ll T_e$.

3 Simulations setup

3.1 Modeling assumptions

Two-fluid, global 3D turbulence codes are used to simulate the TORPEX X-point scenario. Since the ionization fraction in TORPEX plasmas is estimated to be approximately 1%, we consider a

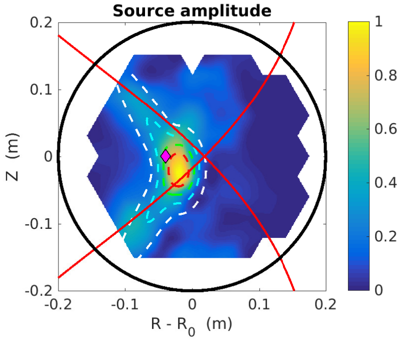

Figure 4: Measured particle source, normalized to its maximum. White, cyan, green and red dashed lines represent the contours of the fitting function $f_S = 0.2$, 0.4, 0.6 and 0.8, respectively. The magenta diamond indicates the position at which simulations are meant to match electron density and temperature.

background of hydrogen molecules with fixed density $n_m = 10^{18}$ m^{-3}, constant in time and space. Electrons can lose momentum not only by electrostatic collisions with ions, but also by collisions with neutrals, in particular with hydrogen molecules. The electron-ion collision time [50] for a hydrogen plasma with $T_e \sim 5$ eV and $n_e \sim 10^{16}$ m^{-3} is $\tau_{ei} \sim 2 \cdot 10^{-5}$ s. The electron-molecule collision time for the mentioned plasma and neutral conditions is shorter, $\tau_{em} \sim 7 \cdot 10^{-6}$ s [51]. Considering this last interaction as the main momentum loss mechanism for electrons, we find that the mean-free path for collisions is $l_{em} = v_{th,e}\tau_{em} \sim 6$ m. As specified in section 2, the connection length $L_\parallel$, measured along the field line from one point on the vessel to the other, is in the range of 10 to 100 m, resulting in a collisionality $\nu^* \equiv L_\parallel / l_{em} \sim 10$. Therefore, first order corrections to the fluid approximation adopted here, such as heat flux limiters, are not expected to be important. The obtained value of collisionality is comparable to the one that can typically be found for electron-ion collisions in a tokamak SOL with $T_e \sim 20$ eV and $n_e \sim 10^{19}$ m^{-3}.

The neutral dynamics is not modelled in this work. Nevertheless, we model plasma-neutral interactions in a simplified manner, taking them into account in friction terms (and also in the parallel heat conduction term in STORM, Appendix A). All the codes accounted only for the dominant electron-molecule collisions, except for STORM, which has taken into account also electron-ion collisions. Since the rate coefficients for electron-atom and electron-molecule elastic collisions are similar (see [52] for ions, [51] for molecules), the impact of considering two different neutral species in our simulations would have been negligible.

The shape of the density source function, Eq. (2.4), has been hard-coded in all the codes. There are no available measurements of the energy source in TORPEX, therefore the latter is imposed in the codes with the same shape as the density source. Notice that GBS and GRILLIX impose an electron temperature source shaped as given by Eq. (2.4), while STORM imposes an energy source of the same shape, see Appendix A. Since there is a large uncertainty in the experimental determination of the amplitude of the sources, we decide to tune the amplitude of the source so that electron density and temperature match the experimental values at a specific point. This point was selected to approximately correspond to the position of the maximum of the measured density and is located at $(R, Z) = (0.96, 0)$ m, as indicated on Figure 4. The values to be matched are $n_e = 2.1 \cdot 10^{16}$ m^{-3} and $T_e = 5.3$ eV. Ions are assumed to be cold ($T_i = 0$).

3.2 Relevant differences between codes

The model and the numerical techniques of each code are presented in detail in Appendix A. The main characteristics of the turbulence codes, in the version used in this work, are summarized in table 2.

	FELTOR	GBS	GRILLIX	STORM
Flux-aligned grid	No	No	No	Yes
Resolution	$972 \times 972 \times 32$	$150 \times 200 \times 32$	$444 \times 504 \times 16$	$96 \times 128 \times 64$
Model	Gyro-fluid	Drift-Fluid	Drift-Fluid	Drift-Fluid
Isothermal	Yes	No	No	No
Electro-magnetic induction	No	No	Yes	No
Boussinesq approximation	No	Yes	No	Yes
Boundary conditions	Simplified	Generalized Bohm	Bohm-Chodura	Bohm-Chodura
Penalization	No	No	Yes	No
Buffer at the boundary	No	Poloidal	Radial	No

Table 2: Characteristic features of the turbulence codes participating in the validation procedure. The reported number of grid points correspond to the horizontal, vertical and toroidal directions for FELTOR, GBS and GRILLIX, and to the radial, poloidal and toroidal directions for STORM.

One of the main differences between the codes is the grid geometry. GBS uses a non-aligned cylindrical grid. GRILLIX and FELTOR use a cylindrical grid, which can be considered as "locally field-aligned"because of the flux-coordinate independent method used to discretize parallel direction [33]. In FELTOR, the grid is a square on the poloidal plane including the whole vacuum vessel, with $R - R_0 \in [-20; 20]$ cm and $Z \in [-20; 20]$ cm, while in GBS, the rectangular domain is vertically cut at approximately the position where the separatrix meets the vessel on the LFS, so $R - R_0 \in [-20; 20]$ cm and $Z \in [-15; 15]$ cm. Both STORM and GRILLIX cut the domain radially at a flux surface corresponding to $R - R_0 \simeq 17$ cm at the midplane. In the poloidal direction GRILLIX cuts the mesh following the direction perpendicular to the flux surfaces, at the most suitable poloidal position to best capture the location of the targets, while the poloidal edge of the STORM grid approximately follows the wall. For all codes, the grid resolution in the poloidal plane is comparable to the sound Larmor radius, which in the conditions explored in this work, is $\rho_s \simeq 2$ mm. STORM constructs field-aligned coordinates using the poloidal angle as the field-line following coordinate, so the very shallow field line pitch in TORPEX means that the parallel resolution is rather compromised, see Appendix A. Nevertheless, all the codes are run with a resolution sufficient to catch the dominant parallel dynamics, which is characterized by low parallel wave numbers. The actual number of points used for the calculations, indicated in Table 2, depends on the numerical schemes adopted by the different codes, that are described in Appendix A.

The codes solve drift-reduced Braginskii equations, except for FELTOR, which solves a set of gyro-fluid equations, thus being able to account for Finite Larmor Radius (FLR) effects. The FLR effects can impact blob properties and thus cross-field turbulent transport [53, 54]. All the codes except FELTOR evolve the electron temperature, while only GRILLIX takes into account electromagnetic induction. GBS and STORM apply the so-called "Boussinesq"approximation to vorticity. The impact of this approximation on SOL turbulence was studied in [55, 56] and its influence on zonal flows in

[57].

Boundary conditions represent also a major difference between the codes. FELTOR uses a simplified set of boundary conditions, which ensure a local particle outflow at the boundary. GBS uses a set of generalized Bohm boundary conditions, derived in [58], at the top and bottom boundaries, allowing in particular currents to flow in and out of the targets. A simplified set of boundary conditions, described in Appendix A, is applied in GBS at the HFS and LFS boundaries, where plasma density is substantially lower than at the X-point, and thus the interaction with the wall is not relevant. In this work, GRILLIX uses a set of Bohm-Chodura boundary conditions [59], which take into account the correction to parallel flows due to $E \times B$ poloidal drift, although it does not allow the flux of electric charge through the boundaries. The "penalization"numerical technique is adopted to apply these conditions, in order to account for complex geometries of the plasma-wall interface [33, 60]. STORM applies $E \times B$ drift-corrected Bohm-Chodura boundary conditions allowing currents at the targets. GBS imposes a buffer region with diffusion coefficients multiplied by a factor 20 in the vicinity of the targets, with a characteristic vertical width of 4 mm, in order to avoid spurious fluxes and limit the perturbations affecting the boundaries. A similar buffer region is imposed in GRILLIX at the radial boundaries, thus far from the strike points. For numerical reasons, GBS simulations in this work are run wit a mass ratio m_i/m_e lower by a factor 6 with respect to reality, and with a constant collisionality in time and space. The impact of collisionality is discussed in Section 5. All the codes except for GRILLIX (see Appendix A for details) assume that turbulence is electrostatic. This assumption is justified by the extremely low values of β reached by TORPEX plasmas.

4 Multi-code simulation results and validation with the experiments

In this section the code results are compared with the experimental data. As a first step, individual profiles of fields of interest are qualitatively compared among the codes and with the experiment. Then, the level of agreement between simulations and experiments is quantified, for a substantial set of observables, using the methods proposed in [23].

4.1 2D comparison of plasma fields and statistical properties

First, we analyze plasma fields averaged over time and toroidal direction. Figure 5 shows the 2D profile of some plasma fields of interest, and the comparison with the experiment. We remark that the experimental data is only averaged in time, since measurements are toroidally localized.

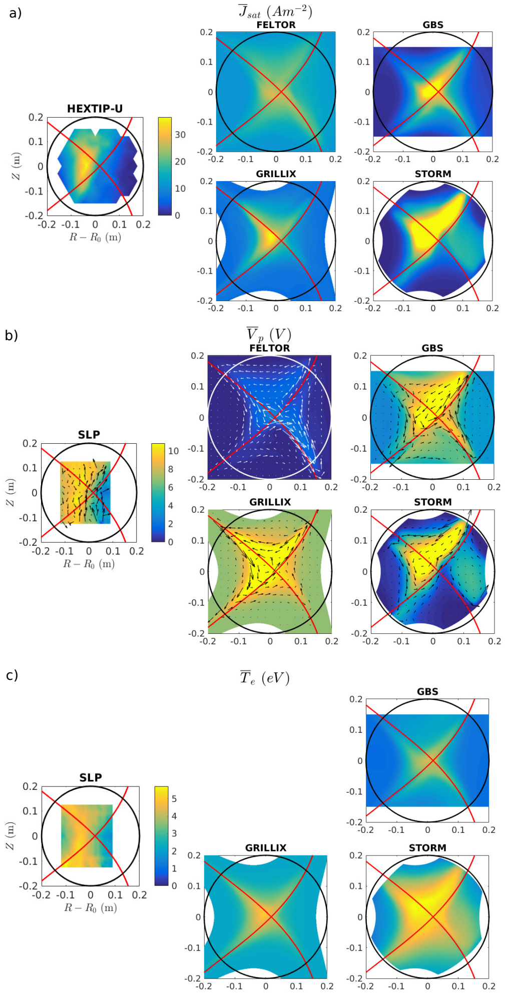

Figure 5: a) On the left, time-averaged ion saturation current density from HEXTIP-U. On the right, ion saturation current density averaged over time and toroidal direction for all the codes. b) Average plasma potential from SLP and from the codes. The arrows represent the $E \times B$ velocity. c) Average electron temperature from SLP and from the anisothermal codes.

As shown in Figure 5a, the ion saturation current peaks near the source location for every code, slightly further towards the LFS than the experiment, with a slight vertical displacement in the upwards direction for STORM and in the downwards direction for FELTOR. Most of the codes can qualitatively reproduce the up-down asymmetry observed in experiments (with the top sector more strongly filled with plasma than the bottom one), although in the simulations the ion saturation current profile is systematically less elongated along the vertical direction. As also seen in Figure 5a, in the simulations, the ion saturation current is substantially larger in the LFS lower branch of the separatrix as compared to the experiment. This suggests an overestimation of the transport across the separatrix in the simulations or differences in the source terms. The plasma potential resulting from simulations, Figure 5b, closely follows the electron temperature spatial distribution, Figure 5c. This is expected as a result of the proportionality between the potential sheath drop and the electron temperature. The electron temperature, Figure 5c, generally shows a field-aligned pattern, although with the formation of relatively strong parallel temperature gradients in GBS and partly in STORM, while the field-alignment seems to be absent in experiments in the top and bottom sectors. Although in simulations the plasma potential is spatially more peaked than in experiments, the strong gradient across the LFS upper branch of the separatrix is well reproduced. This leads to an average $E \times B$ velocity along the same direction as in experiments (see 5b). The comparison of time-averaged $E \times B$ velocities between the simulations and the experiment shows stronger poloidal velocities along the lower LFS separatrix branch, which could contribute to the filling of the LFS sector. Despite this small difference, the overall $E \times B$ velocity pattern found by the codes matches well the experimental one. An analysis of the $E \times B$ particle fluxes is described in Section 4.3. Overall, the simulation results are strongly reminiscent of the source shape and position that have been imposed. In experiments, the marked homogeneity of the profiles in the vertical direction could be due to an effectively more homogeneous source, in particular of energy, than the evaluated one, to some transport mechanism underestimated by the codes, or to an homogenization of the temperature due to electron-neutral collisions.

The integrated power source needed to match the reference density and temperature value in the codes is of the order of 1 W. This quantity is lower by two orders of magnitude with respect to the experimental injected power. This is due to the fact that i) in the experiments, only part of this power is absorbed by the plasma and ii) in simulations we do not include the energy losses to neutrals (ionization and excitation), which represent the main energy loss mechanisms for electrons [49]. Therefore, the power source in our codes only compensates the losses at the walls, which, for realistic plasma parameters, is indeed of the order of 1 W. This calls for new simulations that self-consistently include neutrals, to better model the transport of electron energy.

4.2 1D comparison of radial midplane profiles

The main statistical moments of the ion saturation current density and of the floating potential are calculated for each code, and compared to HEXTIP-U measurements.

As noticeable in Figure 6, the simulations generally show a midplane profile of the ion saturation current density in good agreement with experiments, except for FELTOR, that is characterized by smaller gradients. The level of J_{sat} fluctuations is generally underestimated by all codes, by a factor 2 or more. In particular, the level of fluctuations seems low in the region corresponding to the peak density. We remark that a low level of fluctuations with respect to experiments was obtained also in past simulations of simpler TORPEX configurations [22]. Nevertheless, in the present simulations, the level of fluctuations can reach 40% for all codes near the strike points (not shown here). In the experiment as well as for most of the codes, the skewness of J_{sat} fluctuations is close to zero in the source region and becomes positive in the LFS region, reminiscent of the tokamak Scrape-Off Layer [61]. In simulations, however, the skewness also becomes positive in the HFS region, in clear contrast

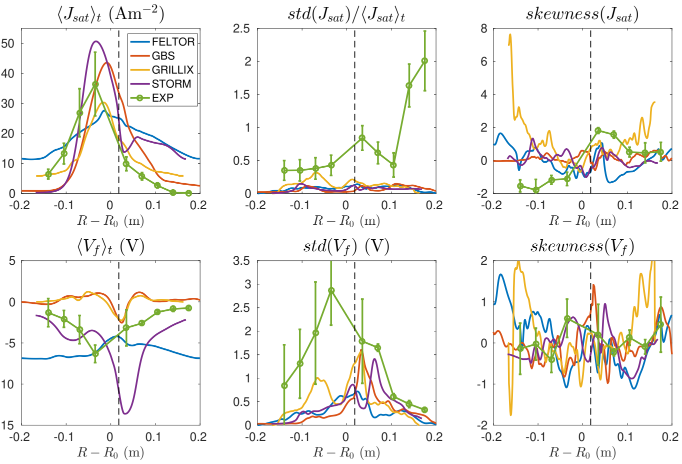

Figure 6: Radial profiles of statistical moments of the ion saturation current density and of floating potential at the midplane ($Z = 0$ cm), compared with experimental data from HEXTIP-U. The vertical dashed line indicates the position of the X-point. The evaluation of the experimental errorbars is explained in Section 4.4.

to the experiment. This is caused by the fact that coherent structures are radially propagating towards the LFS in the experiments, while this propagation can happen also towards the HFS, mainly along the upper separatrix branch, in the simulations.
The codes seem to catch a floating potential negative peak at the separatrix, and a maximum of its fluctuation amplitude, although at the LFS of the X-point instead of its HFS as in experiments. The absolute value of the floating potential is usually not matching well the experiments. One of the possible reasons for this observation is that the electron velocity distribution could differ from a Maxwellian, affecting the sheath potential drop. No trend is clearly visible in the skewness of floating potential fluctuations.

4.3 Blob dynamics and and cross-field transport in simulations

In order to interpret statistical moments of the fluctuations resulting from simulations, it is useful to qualitatively describe the behavior of turbulent structures. Generally, the largest blobs form close to the X-point (most of the time slightly above it, in the top sector), where they are toroidally connected [43]. The turbulent structures get field-aligned further from the X-point, at a similar location as experiments. Examples for each of the codes are shown in Figure 7. In some cases, as for GBS, the blobs stagnate at the same position for some ∼ 10 µs, rotating around their centre. Then, they are expelled from the high-density region, most of the time following the upper LFS branch of the separatrix, as observed in experiments, but sometimes also horizontally across the X-point or along

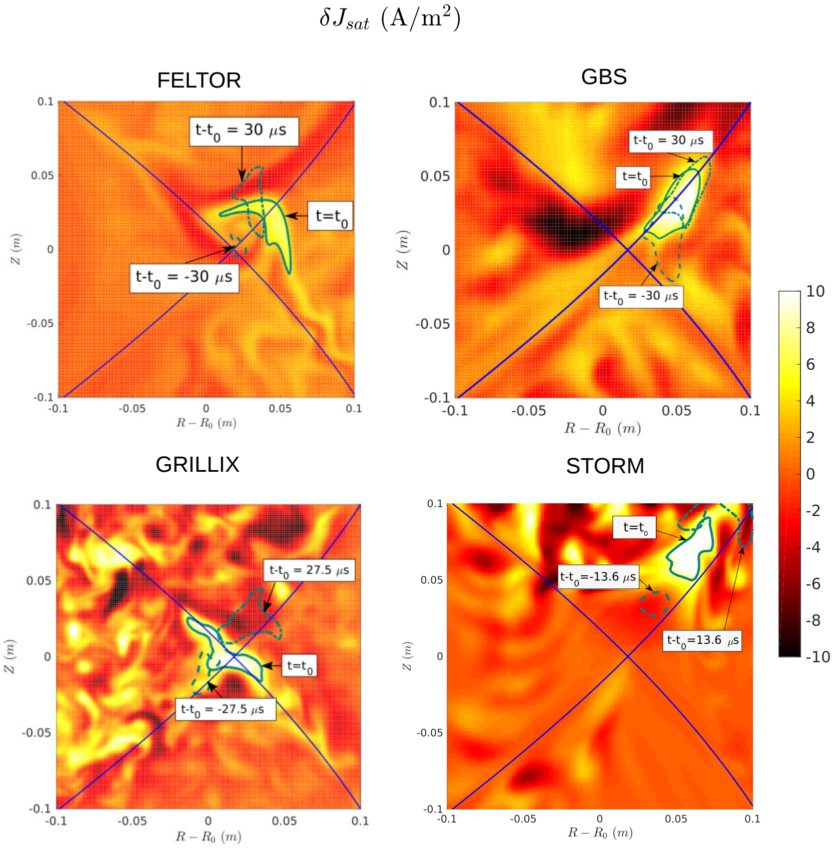

Figure 7: Snapshot of the ion saturation current density fluctuation $\delta J_{sat} = J_{sat} - \overline{J}_{sat}$ (A/m^2) at a chosen time t_0, different for each of the codes (zoom around the X-point region). Dashed, solid and dashed-dotted green lines indicate the blob contour at three different time frames, indicated on the figures. The separatrix is represented in blue.

the other branches of the separatrix. When crossing the separatrix at the LFS, most of the blobs get quickly squeezed along the flux surface, and they are completely damped after some $\sim$ 10 µs. In STORM, the dynamics seems slightly faster than in the other codes, and the blobs are generated at a position slightly further from the X-point (Figure 7). A qualitative comparison with Figure 3a suggests that the blobs detected in the simulations have generally a lower amplitude with respect to experiments, and a smaller cross-section. Additionally, the analysis of the correlation among the ion saturation current signals in HEXTIP1 probes has been performed, then applied also to simulation results. The correlation lengths resulting from this analysis confirm the smaller size of the structures in simulations with respect to the experiment. Wave-like turbulence develops in all codes at flux surfaces further from the X-point, correspondent to a radial position at the midplane of approximately 5 cm $< R - R_0 <$ 10 cm. These structures, which have smaller poloidal extent than the blobs, can interact in a complex way with filaments created near the X-point, sometimes merging with them or affecting their trajectory. Almost no turbulent structures are detected in simulations at the midplane in the far LFS sector ($R - R_0 >$ 10 cm), thus explaining the low level of fluctuations observed in this region (see Figure 6). Overall, the blob dynamics in simulations seems more concentrated near the X-point, and faster by a factor ~ 2 than the experiments, as visible from a qualitative comparison with Figure 3a.

Comparing the $E \times B$ flux associated to fluctuations and to mean-field drifts, we observe that in simulations the background component is clearly dominant, by one order of magnitude, both for the direction across flux surfaces (ψ) and for the poloidal direction (θ). GBS fluxes are shown, as an example, in Figure 8, although all the codes involved in this work similarly show the dominance of the mean-field $E \times B$ fluxes.

It should be noted that, as in the experiments, the local potential dipoles that form within the blobs are comparable to the background potential gradients. The relatively weak $E \times B$ fluxes associated to the fluctuations in the simulations are partly due to the low amplitude of the density fluctuations, and partly to the finite appearance frequency of blobs. In order to compare turbulent fluxes between the codes and the experiment, the discrepancy in the density (or ion saturation current) fluctuation levels must be solved first. Nevertheless, simulations give the clear indication that in the X-point region, the background $E \times B$ fluxes are stronger with respect to the turbulent contribution.

4.4 Validation methodology and results

Following the procedure described in [23], we now quantitatively determine the level of agreement between numerical and experimental results. For each observable j, we evaluate the distance between experimental measurement and simulation as:

$$d_j = \sqrt{\frac{1}{N_j} \sum_{i=1}^{N_j} \frac{\left(x_{i,j} - y_{i,j}\right)^2}{\left(\Delta x_{i,j}\right)^2}} \ , \tag{4.1}$$

where $i = 1, ..., N_j$ are the points at which the value of the observable j is determined, $x_{i,j}$ is its experimental value at the $i - th$ point and $y_{i,j}$ is the simulation result at the same location. We note that every point in the 2D arrays of HEXTIP-U and SLP measurements is considered in the validation. We also note that here we do not consider the errors in simulations, since their rigorous evaluation would require a parameter scan which would be computationally too expensive. Alternatively, an indication on simulation uncertainties introduced by time and space discretization could be given based on the method of the Richardson extrapolation [62], as previously done in [63]. Also this method would be computationally very challenging.

The experimental uncertainty $\Delta x_{i,j}$ is evaluated as:

$$\Delta x_{i,j} = \sqrt{\sum_{k=1}^{N_k} \left(\Delta x_{i,j}^k\right)^2} \ , \tag{4.2}$$

where $k = 1, ..., N_k$ are the different sources of error summarized, for each observable, in Table 3.

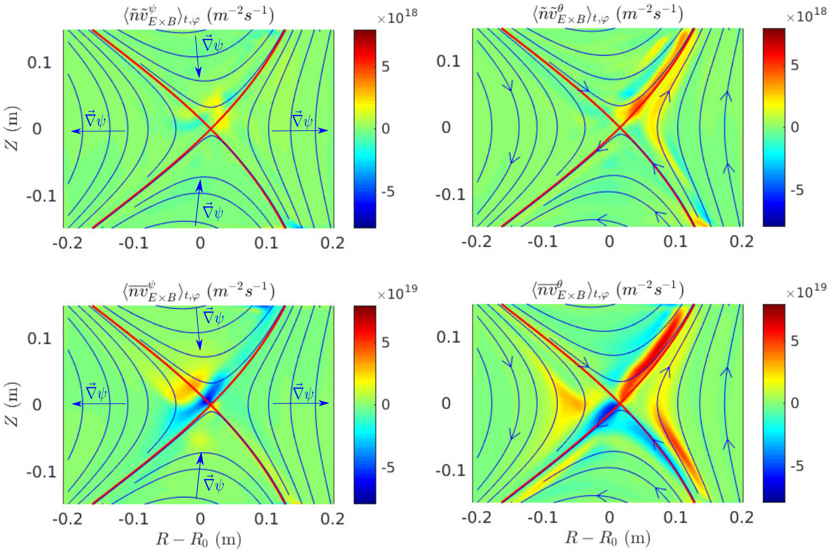

Figure 8: Average in time and toroidal direction of the turbulent and the mean-field components of the $E \times B$ fluxes in the GBS simulation. The $E \times B$ fluxes in the direction ψ across flux surfaces are represented in the left panels, where the arrows indicate the positive ψ direction. The $E \times B$ fluxes in the poloidal direction θ are represented in the right column, where the arrows indicate the positive θ direction. The turbulent and the mean-field components are represented in the top and in the bottom row, respectively. Note the difference in the colorbar between top and bottom row.

For HEXTIP-U data, the repeatability uncertainty is considered as the standard deviation of the measurement over the 44 nominally identical shots included in the experimental dataset and performed within one experimental session. In this way, we quantify the shot-to-shot variability of the time-averaged measurements, within a series of discharges successively performed, with comparable machine conditions. The uncertainty due to machine conditions for each observable is quantified as the difference between the average measurement taken in the reference 44 shots, and the average measurement carried out in a former series of 70 selected shots in the same scenario. Between these two experimental sessions, TORPEX and its diagnostics system underwent some minor upgrades that have slightly influenced the results. SLP measurements were taken only twice for each position during the different experimental sessions, so the machine condition error is calculated as the difference between the two measurements. In the temperature evaluation by SLP, the fitting of the IV curve is also affected by uncertainties. Here we consider different ranges of biasing voltage over which the fitting is performed, then identifying the differences in the fit results as the main source of uncertainty. For this purpose, the minimum temperature fitting approach [64] was applied to two separate voltage ranges, $V \in [V_{f,g}; V_{f,g} + T_{e,g}]$ and $V \in [V_{f,g} + 1.1T_{e,g}; V_{f,g} + 4.5T_{e,g}]$, where $V_{f,g}$ and $T_{e,g}$ are

Observable	Diagnostic	Uncertainty sources	Comparison hierarchy level (Exp.; Sim.)
$\overline{J}_{sat}$	HEXTIP-U	repeatability, machine conditions, probes area	2 (1;2)
$std\left(J_{sat}\right)/\overline{J}_{sat}$	HEXTIP-U	repeatability, machine conditions	2 (1; 2)
$skewness\left(J_{sat}\right)$	HEXTIP-U	repeatability, machine conditions	2 (1; 2)
$\overline{V}_f$	HEXTIP-U	repeatability, machine conditions	2 (1; 2)
$std(V_f)$	HEXTIP-U	repeatability, machine conditions	2 (1; 2)
$skewness(V_f)$	HEXTIP-U	repeatability, machine conditions	2 (1; 2)
$\overline{V}_p$	SLP	machine conditions, IV curve fitting	2 (2; 1)
$\overline{n}$	SLP	machine conditions, IV curve fitting, probes area	2 (2; 1)
$\overline{T}_e$	SLP	machine conditions, IV curve fitting	2 (2; 1)

Table 3: List of observables with corresponding diagnostics and sources of uncertainty. The experiment, simulation and comparison hierarchy levels are also reported for each observable.

initial guess values for V_f and T_e, respectively. This uncertainty also affects density, which is derived from J_{sat} and T_e measurements. Measurements of J_{sat} (HEXTIP-U) and n (SLP), are affected by an uncertainty on the probe tip collecting areas. In the calculation of the level of fluctuations and of the skewness of J_{sat}, however, this uncertainty averages out. The absolute value of density, and thus also of ion saturation current, is scaled here, homogeneously over all points, in order to obtain a calculated position of the UH resonance, Eq. (2.3), consistent with the peak of the source shape shown in Figure 4. The uncertainty is thus due to the limited spatial resolution of HEXTIP-U in the source measurements, which translates in an uncertainty in the upper-hybrid density.
Following Ref. [23], we quantify the combined experimental and numerical precision in the evaluation of the observable j by the parameter S_j, defined as:

$$S_j = \exp\left(-\frac{\sum_i \Delta x_{i,j}}{\sum_i |x_{i,j}| + \sum_i |y_{i,j}|}\right) \ . \tag{4.3}$$

Also, based on the evaluated distances d_j, the simulation-experiment agreement for each observable j is quantified by the function R_j, defined as:

$$R_j = \frac{1}{2}\left[\tanh\left(\frac{d_j - 1/d_j - d_0}{\lambda}\right) + 1\right] \ , \tag{4.4}$$

where d_0 is a reference distance marking the transition from agreement to disagreement, and λ is an arbitrary parameter characterizing the steepness of the agreement function R_j, thus determining how fast one result passes from being considered in agreement to being considered in disagreement. In this work, we impose $d_0 = 1$, corresponding to the case where the distance of the numerical result from the experiment coincides with the amplitude of the errorbar. We further set $\lambda = 0.5$ as in the previous validation work [65].
Each observable is associated with an experimental hierarchy level and a simulation hierarchy level. Every independent measurement or functional model combining several measurements adds one unit to the hierarchy level [22]. For each observable j, these two hierarchy levels are combined together in a comparison hierarchy level h_j. The hierarchy levels are reported in Table 3. A weight $H_j = 1/h_j$ is associated to each observable, so that the lowest levels are the most important in the validation procedure. In this work, we focus on observables with low hierarchy level, which are the most direct

measurements, and thus also the most important to be matched by simulations. The quality of the comparison is then calculated as:

$$Q = \sum_j H_j S_j \ , \tag{4.5}$$

and it is a measure of how stringent or extensive the validation is [22], increasing with the number of observables and with their precision, and decreasing with their hierarchy level. The overall level of agreement between a simulation and the experiment, or "metric", is defined as:

$$\chi = \frac{\sum_j R_j H_j S_j}{\sum_j H_j S_j} \ , \tag{4.6}$$

where $\chi \in [0;1]$, $\chi = 0$ indicating perfect agreement and $\chi = 1$ no agreement. When applying the validation procedure to FELTOR, which is isothermal, electron temperature is excluded from the list of observables. The time-averaged floating potential is also excluded, since it is calculated as $V_f = \phi - \Lambda T_e$, so through a model of the sheath dependent on T_e, which is not applicable to FELTOR simulations. Moreover, for FELTOR we calculate the statistical moments of the plasma potential ϕ instead of the floating potential V_f, since in an isothermal model these fields differ only by a constant. The results of the validation procedure for each code are reported Table 4.

	FELTOR	GBS	GRILLIX	STORM	GBS $\nu^\star \times 3.5$ R_S=0.90m	GBS $\nu^\star \times 3.5$ R_S=0.95m	GBS $\nu^\star \times 3.5$ R_S =0.98m
$\overline{J}_{sat}$	46.5	14.5	20.6	17.85	26.7	11.3	19.9
$std(J_{sat})/\overline{J}_{sat}$	6.76	2.77	2.73	2.68	3.00	2.84	2.14
$skewness(J_{sat})$	3.91	4.27	9.42	4.93	23.3	21.1	4.72
$\overline{V}_f$	🟩	8.39	6.77	8.58	7.33	9.65	14.9
$std(V_f)$	70.9	5.76	6.11	5.22	8.06	7.40	6.40
$skewness(V_f)$	3.27	2.50	8.69	2.75	22.2	18.8	2.35
$\overline{V}_p$	3.06	1.28	1.33	1.60	1.26	2.35	1.62
$\overline{n}_e$	5.02	3.85	1.72	4.75	2.67	1.86	2.68
$\overline{T}_e$	🟩	4.02	2.63	2.35	2.75	1.72	3.38
Q	2.86	3.50	3.63	3.54	3.72	3.74	3.58
χ	1.00	0.89	0.85	0.93	0.90	0.93	0.93

Table 4: Distance d_j evaluated for all the observables in all the simulations. A green color indicates a good agreement, while the more the background color tends to the red, the larger the disagreement. The colorscale is saturated at 5, and empty fields correspond to quantities not simulated by the code. The last two lines indicate the quality Q and the metric χ for each simulation. The last three columns are referred to the simulations discussed in Section 5.

Globally, the agreement between numerical and experimental results, identified by the metric χ, is not satisfactory from a quantitative point of view, as visible in Table 4. We remark here, however, that not considering numerical errorbars makes this comparison particularly strict with respect to previous validation works (e.g. [23, 25]). FELTOR, GBS, GRILLIX and STORM simulations result in a level of agreement of $\chi \simeq 1.00, 0.89, 0.85$ and 0.93, respectively. The observables determining these differences between codes are mainly the average density, temperature and plasma potential, where the distance between codes and experiments is within a few (~ 2) errorbars. The distance between simulations and experiments is generally lower, and hence the agreement better, for the observables evaluated with SLP measurements ($\overline{V}_p$, $\overline{n}_e$ and $\overline{T}_e$), with respect to the ones derived by HEXTIP-U (the statistical moments of J_{sat} and V_f). We note, however, that the comparison with quantities measured by HEXTIP-U is more stringent, as it involves a larger number of measurement points. Although the validation results are quantitatively not satisfactory, we note here that the application of the metric is a useful tool to assess, in an objective manner, how much the agreement can be improved in future, more refined simulations. In addition, this quantitative evaluation allows to assess the sensitivity of the simulation results to certain input parameters. Such an analysis is performed in the next section.

5 Sensitivity to the source position and collisionality

Simulation results appear to be strongly dependent on the source terms (columns 3 and 4 in Figure 9). Moreover, the experimental assessment of the source includes several approximations and assumptions. For instance, the limited spatial resolution of HEXTIP-U, which is used for the source evaluation, as well as the imperfect control on the X-point position, can lead to an uncertainty on the radial source position $\Delta R_S \sim 4$ cm. The collisionality, evaluated from experiments, is a parameter also affected by large uncertainties. In particular, the time-average resistivity in the reference point, derived with the Braginskii model, can vary by up to a factor 4, considering the uncertainties on electron density and temperature measurements. Therefore, three additional GBS simulations have been performed, where the radial coordinate of the density and temperature source center R_S has been scanned, keeping all the other source parameters fixed, including the vertical position and the intensity of the source. The collisionality has instead been increased by a factor 3.5 in this scan, which allows computational time to be saved. This results in an increase of the parallel resistivity by a factor 3.5 and in a decreased parallel heat conductivity by the same factor, according to Braginskii estimates [50]. Therefore, these simulations allow us to test also the sensitivity of the results, and of the metric χ, on these parameters. The simulated values of source radial position R_S are $[0.90; 0.95; 0.98]$ m, where $R_S = 0.98$ m is the value used in the simulations discussed in Section 4. The validation procedure is applied to these additional simulations and its results are included in Table 4.

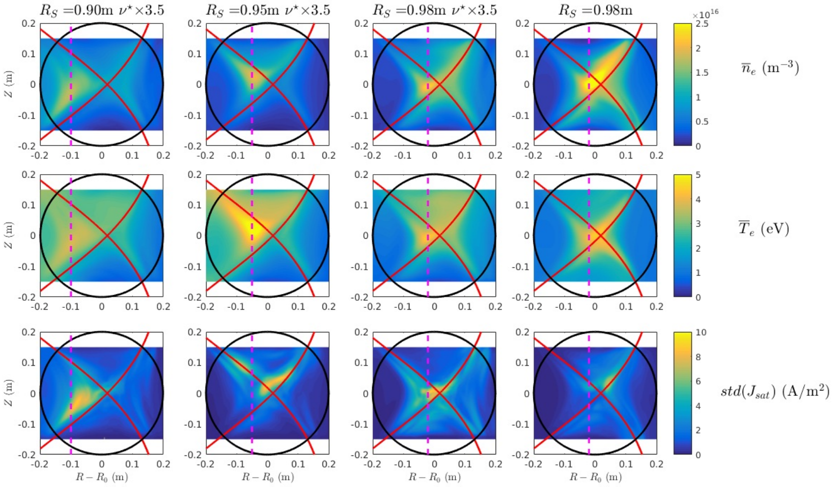

Figure 9: First row: plasma density in three GBS simulations with particle source at $R_S = [0.90; 0.95; 0.98]$ m and increased collisionality. The center of the source is identified by a vertical dashed line. The fourth column shows the reference GBS simulation with collisionality set to the Braginskii value. Second row: the same for electron temperature. Third row: standard deviation of the ion saturation current.

We compare first the two simulations with $R_S = 0.98$ m, but with different collisionalities. We notice that the density profiles at the outer midplane are broader in the high collisionality case (Figure 9, third column) with respect to the reference case (Figure 9, fourth column), as a consequence of the increased resistivity. The higher collisionality leads to less field-aligned temperature as expected from the lower parallel heat conductivity, and in general to a dynamics less concentrated along the separatrix. Nevertheless, as visible from Table. 4, the floating and plasma potential show a higher global disagreement with experiment at high collisionality, leading to an increase in metric $\Delta\chi \sim 0.05$. As the source moves further from the X-point, the average density and temperature peaks follow its radial position, as visible in Figure 9 (first two rows). The lower LFS separatrix leg, nevertheless, shows similar values of density and temperature in all cases. The behavior of turbulent structures also qualitatively changes with the source position. As shown in Figure 9 (last row), the fluctuations with the largest amplitude occur close to the source center, where the density peaks, and in particular on its low field side. However, the further left the source is, the more the fluctuations tend to propagate also to the HFS. In the case $R_S = 0.95$ m, some blobs seem to spread in the top sector, increasing density and temperature homogeneity there, and thus slightly improving the agreement with experiments on these observables (see Table 4) with respect to the case with $R_S = 0.98$ m. Nevertheless, the peak of the fluctuation level is displaced with respect to the experimental one, so the agreement on statistical moments gets worse. Globally, the resulting level of agreement is similar to the case with $R_S = 0.98$ m. In the case with $R_S = 0.90$ m, the plasma strongly interacts with the HFS wall, and the structures are mainly directed towards the HFS strike points, clearly in contrast with the experiment. Nevertheless, the resulting plasma potential, more homogeneous in the HFS and top sectors, leads to a metric close to the reference case.

Globally, the dynamics shown by the reference simulation best approaches the blob dynamics observed in experiments, with turbulent structures propagating principally along the upper LFS branch of the separatrix. The time-averaged plasma potential seems to be best reproduced in this case, globally leading to the best χ values found among GBS simulations. This analysis increases the confidence in our experimental evaluation of the source position and collisionality. Moreover, it reveals that the uncertainties on these parameters can mildly affect the global level of agreement, with a change of $\Delta\chi/\chi \sim 0.05$.

6 Conclusions

Previous multi-code validation studies of edge plasma turbulence, carried out with 3D fluid turbulence codes, have been extended in this work to an X-point configuration in the basic plasma device TORPEX, where the plasma is widely accessible by Langmuir probe arrays. For this purpose, a new TORPEX experimental scenario, featuring a magnetic null but no closed field lines, has been developed. The poloidal field is scanned, and an intermediate value is chosen for the reference experimental scenario, to have, at the same time, a relatively high blob generation rate and a magnetic shear induced by the X-point comparable to the one in a tokamak. Langmuir probe arrays measurements show that both the local potential dipole and the background plasma potential affect transport of turbulent structures. Therefore, the newly developed TORPEX scenario includes the main elements that need to be described by 3D fluid turbulence codes in the X-point region.

This X-point scenario was simulated with FELTOR, GBS, GRILLIX and STORM. Despite being computationally relatively inexpensive, the simulations have proven to be challenging for all the codes involved in this work, mainly because of the shallow incidence angle at the vessel, and the high level of fluctuations near the boundaries. A further complication with respect to previous validations on TORPEX is the intrinsic 2D nature of the problem on the poloidal plane, given by the geometric structure of the X-point. In this framework, the flexibility of the codes, which are essentially built for tokamak simulations, has been severely tested, in order to cope with the complex magnetic geometry and the peculiar source shape.

The simulations are qualitatively and quantitatively compared to the experiments, using the procedure detailed in [65]. The qualitative comparison shows that the codes are able to reproduce key time-average features of the scenario, as the up-down asymmetry, the ion saturation current profiles at mid-height and the blob trajectories. The quantitative validation shows that, in particular, the average plasma potential, and thus the background $E \times B$ velocities, are reproduced within 1 to 2 errorbars, where the latter account for experimental uncertainties due to repeatability, machine conditions and area of the Langmuir probe tips. An interesting observation in these simulations is the clear dominance of fluxes due to background $E \times B$ drifts over those due to fluctuations, both in radial and poloidal directions. Therefore, in these simulations the background fluxes determine the average profiles. The sensitivity of the results on the source position and the plasma collisionality was quantitatively assessed with additional GBS simulations. Varying these parameters in a range compatible with experimental uncertainties led to a mild variation in the metric, a measure of the global agreement between simulations and experiments, by $\Delta\chi/\chi \sim 0.05$.

Some key discrepancies between simulations and experiments have been proven hard to reconcile. Simulations generally underestimate the level of fluctuations, as observed in earlier TORPEX validations, and by consequence also the turbulent transport. The floating potential is generally not well described, as well as the homogeneity of profiles in the vertical direction. The inclusion of a self-consistent description of neutral dynamics seems to be mandatory in order to improve the agreement between simulations and experiments. In particular, the inclusion of electron energy losses by ionization, excitation, dissociation and other relevant atomic and molecular processes which are neglected at the moment, could improve the agreement in the average temperature profiles. Turbulence could also be altered by the vorticity damping due to ion-neutral collisions. The X-point simulations would also benefit from a more refined description of the microwave absorption by the plasma, which is a complex dynamic process that determines the effective density and energy sources. The implementation of boundary conditions adapted to low-incidence angles would also be expected to improve the description of the X-point scenario.

The present work is part of a multi-step validation process of the 3D fluid edge turbulence codes, and paves the way for similar studies in diverted tokamak scenarios [66]. However, tokamaks are more complex, and less accessible systems with respect to basic plasma devices, leading to a higher difficulty of the validation exercise. The TORPEX X-point scenario is therefore important itself as a benchmark for future improvements in the modelling. For instance, the inclusion of models for neutral dynamics that are recently being coupled to turbulence codes (e.g. [67, 36]) could be tested on the TORPEX X-point scenario, with a relatively low computational effort. The application of the same validation procedure as performed in this work will allow a quantitative and objective assessment of the effect of such improvements in modelling.

Supplementary Material

See supplementary material for a visual representation of the temporal evolution of the ion saturation current density fluctuations in a TORPEX poloidal plane, resulting from FELTOR, GBS, GRILLIX and STORM simulations.

Acknowledgments

This work has been carried out within the framework of the EUROfusion Consortium and has received funding from the Euratom research and training programme 2014-2018 and 2019-2020 under grant agreement number 633053. The views and opinions expressed herein do not necessarily reflect those of the European Commission. This work was supported in part by the Swiss National Science Foundation. This work has also been part-funded by the RCUK Energy Programme [grant number EP/T012250/1]. GBS simulations were performed on the CINECA Marconi supercomputer within the framework of the FUA34 DIVturb project. This work was supported by a grant from the Swiss National Supercomputing Centre (CSCS) under project IDs s1028 and s882. We acknowledge PRACE for awarding us access to SuperMUC-NG at GCS@LRZ, Germany. GRILLIX simulations were performed on the MPCDF Draco cluster and on the CINECA Marconi supercomputer within the framework of the FUA34 EST3D project. STORM simulations were performed on the CINECA Marconi supercomputer within the framework of the FUA33 SOLBOUT3, FUA34 SOLBOUT4, and FUA35 SOLBOUT5 projects.

Data availability

The data that support the findings of this study are available from the corresponding author upon reasonable request.

Appendix A Turbulence codes model

In the following sections, we present in detail the physical models solved in this work by the different turbulence codes. In all the models, the notation is the following:

- n : plasma density ,
- ϕ : plasma potential ,
- T_e : electron temperature ,
- p_e : electron pressure ,
- $v_{\|e}$: electron parallel velocity ,
- $v_{\|i}$: ion parallel velocity ,
- ω : vorticity ,
- $j_\|$: parallel current.

The models are reported here in SI units, although the codes solve conveniently normalized equations. Additional quantities specific to each code are defined in the corresponding section.

A.1 FELTOR

For this study we use an isothermal 3D gyro-fluid model that includes Finite Larmor Radius effects down to the gyro-radius, but polarization effects in the long wavelength approximation [68, 69, 70, 71]. The latter approximation has been relaxed only recently [72]. The perpendicular derivatives in the gyro-fluid model are discretized in a discontinuous Galerkin framework, which couples to an FCI expression for the parallel derivatives [54]. The FCI approach bases on finite-differences along the magnetic fieldlines and makes use of the Legendre polynomial expansion in the discontinuous Galerkin representation to obtain the necessary grid interpolations. The model is implemented in the FELTOR library [32]. This library features platform independent algorithms implemented using modern C++ template meta-programming techniques and thus allows to run the code on a multi-GPU hardware architecture. The use of binary reproducible scalar products makes the code both reproducible and accurate.

In cylindrical coordinates and dimensionless units the general axisymmetric magnetic field can be written as

$$\boldsymbol{B} = \frac{R_0}{R}\left[I(\psi_p)\hat{\mathbf{e}}_\varphi + \frac{\partial \psi_p}{\partial Z}\hat{\mathbf{e}}_R - \frac{\partial \psi_p}{\partial R}\hat{\mathbf{e}}_Z\right], \tag{A.1}$$

FELTOR uses an analytical expression for $I(\psi_p)$ and ψ_p given by Reference [73]. Further, FELTOR uses a toroidal/negative toroidal field line approximation. This applies $\mathbf{b} \approx \pm\hat{\mathbf{e}}_\varphi$ to all perpendicular terms ($E \times B$ drift, perpendicular elliptic operator and curvature operators) but retains the full expression for the magnetic field unit vector $\mathbf{b}$ for parallel derivatives ($\nabla_\| := \mathbf{b}\cdot\boldsymbol{\nabla}$ and $\Delta_\| = \boldsymbol{\nabla}\cdot\mathbf{b}\mathbf{b}\cdot\boldsymbol{\nabla}$). Note that a negative sign $-\hat{\mathbf{e}}_\varphi$ enables a sign reversal of the magnetic field.

In cylindrical coordinates that is

$$\boldsymbol{\nabla}_\perp f = \partial_R f\hat{\mathbf{e}}_R + \partial_Z f\hat{\mathbf{e}}_Z \tag{A.2}$$

$$\Delta_\perp f = \frac{1}{R}\partial_R\left(R\partial_R f\right) + \partial_Z(\partial_Z f) \tag{A.3}$$

The curl of $\mathbf{b}$ reduces to $\boldsymbol{\nabla}\times\mathbf{b} = -\frac{\pm 1}{R}\hat{\mathbf{e}}_Z$. This simplifies the curvature operators to:

$$\boldsymbol{K}_{\boldsymbol{\nabla}\times\mathbf{b}} = -\frac{\pm 1}{BR}\hat{\mathbf{e}}_Z, \qquad \boldsymbol{K}_{\boldsymbol{\nabla}B} = -\frac{\pm 1}{B^2}\frac{\partial B}{\partial Z}\hat{\mathbf{e}}_R + \frac{\pm 1}{B^2}\frac{\partial B}{\partial R}\hat{\mathbf{e}}_Z \qquad \boldsymbol{K} = \boldsymbol{K}_{\boldsymbol{\nabla}B} + \boldsymbol{K}_{\boldsymbol{\nabla}\times\mathbf{b}}, \tag{A.4}$$

which results in a vanishing divergence of the curvature operator $\boldsymbol{\nabla}\cdot\boldsymbol{K} = 0$.

The model equations comprise the continuity equation for the electron density $n_e \equiv n$, the ion gyro-centre density N_i, the velocity equations for the parallel electron velocity $u_{\parallel,e} \equiv v_{\parallel,e}$ and the parallel ion gyro-centre velocity $U_{\parallel,i}$. Note that the electron gyro-centre quantities coincide with their drift-fluid counterparts due to vanishing gyro-radius. In contrast the ion gyro-centre quantities N_i and $U_{\parallel,i}$ require a transformation back to particle space in order to compare to n and $v_{\parallel,i}$. Omitting species labels the model reads

$$\frac{\partial}{\partial t}N + \boldsymbol{\nabla}\cdot\left(N\left(\boldsymbol{v}_E + \boldsymbol{v}_K + \boldsymbol{v}_C + U_\parallel \mathbf{b}\right)\right) = -\nu_\perp \Delta_\perp^2 N + S_N \tag{A.5}$$

$$\begin{aligned} mN\frac{\partial}{\partial t}U_\parallel &+ mN\left(\boldsymbol{v}_E + \boldsymbol{v}_K + \boldsymbol{v}_C + U_\parallel \mathbf{b}\right)\cdot\boldsymbol{\nabla}U_\parallel \\ &+ 2m\boldsymbol{\nabla}\cdot\left(NU_\parallel \boldsymbol{v}_{\nabla\times\mathbf{b}}\right) - mNU_\parallel \boldsymbol{\nabla}\cdot\boldsymbol{v}_{\nabla\times\mathbf{b}} + mNU_\parallel \mathcal{K}_{\nabla\times\mathbf{b}}(\psi) \\ &= -T\nabla_\parallel N - qN\nabla_\parallel \psi + qn\eta_\parallel j_\parallel \\ &+ \nu_\parallel \Delta_\parallel U_\parallel + mN\left(-\nu_\perp \Delta_\perp^2 U_\parallel\right) + mU_\parallel\left(-\nu_\perp\Delta_\perp^2 N + S_N\right) \end{aligned} \tag{A.6}$$

with the $E \times B$ and curvature drift velocities

$$\boldsymbol{v}_E := \frac{\hat{\mathbf{e}}_\varphi \times \nabla\psi}{B}, \quad \boldsymbol{v}_K := \frac{T}{q}\boldsymbol{K}, \quad \boldsymbol{v}_C := \frac{mU_\parallel^2}{q}\boldsymbol{K}_{\boldsymbol{\nabla}\times\mathbf{b}}, \quad \boldsymbol{v}_{\nabla\times\mathbf{b}} := \frac{T}{q}\boldsymbol{K}_{\boldsymbol{\nabla}\times\mathbf{b}}. \tag{A.7}$$

with $q_e = -e$ and $q_i = +e$.

The electric potential ϕ is computed by the polarization equation

$$-\boldsymbol{\nabla}\cdot\left(\frac{m_i N_i}{eB^2}\boldsymbol{\nabla}_\perp \phi\right) = \Gamma_{1,i}N_i - n_e, \quad \Gamma_{1,i}^{-1} := 1 - \frac{m_i T_i}{2e^2 B_0^2}\Delta_\perp, \tag{A.8}$$

given ϕ the generalized electric potential is defined as

$$\psi_e := \phi, \quad \psi_i := \Gamma_{1,i}\phi - \frac{m_i}{2e}\left(\frac{\boldsymbol{\nabla}_\perp \phi}{B}\right)^2. \tag{A.9}$$

The parallel Spitzer resistivity (applied to current $j_\parallel = en_e(U_{\parallel,i} - u_{\parallel,e})$ is

$$\eta_\parallel := \frac{0.51 m_e \nu_{ei}}{n_e e^2} \tag{A.10}$$

while $\nu_\parallel$ and $\nu_\perp$ are numerically motivated parameters that stabilize the simulation.
The model uses Dirichlet boundary conditions for the electric potential and the density and homogeneous Neumann boundary conditions for the velocity.

A.2 GBS

GBS [74, 9] is a three-dimensional, flux-driven, global turbulent code used to simulate plasma turbulence in basic plasma devices as well as in the boundary of tokamaks. By assuming the Boussinesq [74, 75] and the large-aspect ratio approximations, the equations implemented in GBS in the cold ions and electrostatic limits are

$$\frac{\partial n}{\partial t} = -\frac{1}{B}\left[\phi, n\right] + \frac{2}{eB}\Big[C(p_e) - enC(\phi)\Big] - \nabla_\parallel(nv_{\parallel e}) + D_n\nabla_\perp^2 n + S_n\,, \tag{A.11}$$

$$\frac{\partial \omega}{\partial t} = -\frac{1}{B}\left[\phi, \omega\right] - v_{\parallel i}\nabla_\parallel\omega + \frac{B\Omega_{ci}}{en}\nabla_\parallel j_\parallel + \frac{2\Omega_{ci}}{en}C(p_e) + D_\omega\nabla_\perp^2\omega\,, \tag{A.12}$$

$$\frac{\partial v_{\parallel e}}{\partial t} = -\frac{1}{B}\left[\phi, v_{\parallel e}\right] - v_{\parallel e}\nabla_\parallel v_{\parallel e} + \frac{e}{m_e}\Big(\frac{j_\parallel}{\sigma_\parallel} + \nabla_\parallel\phi - \frac{1}{en}\nabla_\parallel p_e - \frac{0.71}{e}\nabla_\parallel T_e\Big)$$

$$+\frac{4\eta_{0,e}}{3nm_e}\nabla_\parallel^2 v_{\parallel e} + D_{v_{\parallel e}}\nabla_\perp^2 v_{\parallel e}\,, \tag{A.13}$$

$$\frac{\partial v_{\parallel i}}{\partial t} = -\frac{1}{B}\left[\phi, v_{\parallel i}\right] - v_{\parallel i}\nabla_\parallel v_{\parallel i} - \frac{1}{m_i n}\nabla_\parallel p_e + \frac{4\eta_{0i}}{3nm_i}\nabla_\parallel^2 v_{\parallel i} + D_{v_{\parallel i}}\nabla_\perp^2 v_{\parallel i}\,, \tag{A.14}$$

$$\frac{\partial T_e}{\partial t} = -\frac{1}{B}\left[\phi, T_e\right] - v_{\parallel e}\nabla_\parallel T_e + \frac{2}{3}T_e\Big[0.71\nabla_\parallel v_{\parallel i} - 1.71\nabla_\parallel v_{\parallel e} + 0.71(v_{\parallel i} - v_{\parallel e})\frac{\nabla_\parallel n}{n}\Big]$$

$$+\frac{4}{3}\frac{T_e}{eB}\Big[\frac{7}{2}C(T_e) + \frac{T_e}{n}C(n) - eC(\phi)\Big] + D_{Te}\nabla_\perp^2 T_e + \chi_{\parallel e}\nabla_\parallel^2 T_e + S_{T_e}\,, \tag{A.15}$$

$$\nabla_\perp^2\phi = \omega \tag{A.16}$$

where $\Omega_{ci} = eB/m_i$ is the ion cyclotron frequency. The spatial operators appearing in Eqs. (A.11)-(A.16) are the $E \times B$ advection operator $\big[\phi, f\big] = \mathbf{b} \cdot (\nabla\phi \times \nabla f)$, the curvature operator $C(f) = B\big[\nabla \times (\mathbf{b}/B)\big]/2 \cdot \nabla f$, the parallel gradient operator $\nabla_\parallel f = \mathbf{b} \cdot \nabla f$, and the perpendicular Laplacian operator $\nabla_\perp^2 f = \nabla \cdot \big[(\mathbf{b} \times \nabla f) \times \mathbf{b}\big]$, where $\mathbf{b} = \mathbf{B}/B$ is the unit vector of the magnetic field. The operators are derived in the large aspect ratio approximation.

The physical parameters appearing in the model equations are the electron and ion viscosities, $\eta_{0,e}$ and $\eta_{0,i}$, the electron parallel thermal conductivity $\chi_{\parallel e}$, the parallel electric conductivity, $\sigma_\parallel$, and the perpendicular diffusion coefficients $D_{n/\omega/v_{\parallel e}/v_{\parallel i}/T_e}$. In this work, we assume that the dominant momentum loss mechanism is due to electron-molecules collisions, which leads to a parallel conductivity of $\sim$ 770 S/m [51]. The magnetic presheath boundary conditions, derived in Ref. [58], are applied at the top and bottom walls of the domain. In the (R, φ, Z) cylindrical coordinates and neglecting correction terms linked to radial derivatives of density and electrostatic potential at the target plates, the boundary conditions are written as

$$v_{\parallel i} = \pm\, c_s, \tag{A.17}$$

$$v_{\parallel e} = \pm\, c_s \;\exp\Big(\Lambda - e\frac{\phi}{T_e}\Big), \tag{A.18}$$

$$\frac{\partial}{\partial Z}n = \mp\,\frac{n}{c_s}\frac{\partial}{\partial Z}v_{\parallel i}, \tag{A.19}$$

$$\frac{\partial}{\partial Z}\phi = \mp\,\frac{m_i c_s}{e}\frac{\partial}{\partial Z}v_{\parallel i}, \tag{A.20}$$

$$\frac{\partial}{\partial Z}T_e = 0, \tag{A.21}$$

$$\omega = -\frac{m_i}{e}\left[\big(\frac{\partial}{\partial Z}v_{\parallel i}\big)^2 \mp c_s\,\frac{\partial^2}{\partial Z^2}v_{\parallel i}\right], \tag{A.22}$$

where $\Lambda = 3.1$ in TORPEX simulations, and $c_s = \sqrt{eT_e/m_i}$. The top (bottom) sign refers to the magnetic field pointing towards (away from) the target plate. A set of simplified boundary conditions is applied at the HFS and LFS boundaries, where the plasma-wall interaction is weak. At these boundaries, the radial gradients of n, T_e, $v_{\parallel e}$ and $v_{\parallel i}$ are set to 0, while $\omega = 0$ and $\phi = \Lambda T_e$ are

PLEASE CITE THIS ARTICLE AS DOI: 10.1063/5.0064522

imposed.

The differential operators appearing in Eqs. (A.11)-(A.16) are discretized on a non-field aligned Cartesian grid by using a fourth-order finite differences scheme [9]. The Poisson brackets operators are discretized by means of a fourth-order Arakawa scheme. Time is advanced by using a standard fourth-order Runge-Kutta scheme. Details on the numerical implementation are reported in Refs. [9, 21, 67]. The GBS domain has been recently extended to include the whole plasma volume when simulating a tokamak [35]. GBS has been verified with the method of manufactured solutions [63] and extensively validated with a rigorous validation methodology [23] against experimental results [74, 65, 25].

A.3 GRILLIX

GRILLIX [76, 33] is a 3D Braginskii-fluid turbulence code which, like FELTOR, uses the 'flux-coordinate independent' method to discretize the parallel dynamics, and standard second-order finite differences to discretize the perpendicular dynamics. For this study we use the model presented in Stegmeir et al, 2019 [33], which is a set of non-Boussinesq, drift-reduced Braginskii equations. There is no separation of the background and fluctuations of the solved fields, except for the current associated with the background magnetic field. Electromagnetic induction is present in Ohm's law, but magnetic 'flutter' terms, causing electromagnetic transport are disabled.

$$\frac{d}{dt}n = n\mathcal{K}(\phi) - \frac{n}{e}\mathcal{K}(T_e) - \frac{T_e}{e}\mathcal{K}(n) + \nabla\cdot\left[\left(\frac{j_\parallel}{e} - nv_{\parallel i}\right)\mathbf{b}\right] + \mathcal{D}_n(n) + S_n, \tag{A.23}$$

$$\nabla\cdot\left[\frac{m_i n}{B^2}\left(\frac{d}{dt} + v_{\parallel i}\nabla_\parallel\right)\nabla_\perp\phi\right] = -T_e\mathcal{K}(n) - n\mathcal{K}(T_e) + \nabla\cdot\left(j_\parallel\mathbf{b}\right) + \mathcal{D}_\omega(\omega), \tag{A.24}$$

$$m_i n\left(\frac{d}{dt} + v_{\parallel i}\nabla_\parallel\right)v_{\parallel i} = -\nabla_\parallel p_e + \mathcal{D}_u(u_\parallel), \tag{A.25}$$

$$-\frac{m_e}{e}\left(\frac{d}{dt} + v_{\parallel e}\nabla_\parallel\right)\frac{j_\parallel}{en} - \frac{\partial}{\partial t}A_\parallel = \frac{0.51 m_e}{e^2\tau_{en}}j_\parallel + \nabla_\parallel\phi - \frac{1}{en}\nabla_\parallel p_e - 0.71\frac{1}{e}\nabla_\parallel T_e + \mathcal{D}_\Psi(\Psi_m), \tag{A.26}$$

$$\begin{aligned}\frac{3}{2}\left(\frac{d}{dt} + v_{\parallel e}\nabla_\parallel\right)T_e &= -\frac{7}{2}\frac{T_e}{e}\mathcal{K}(T_e) - \frac{T_e^2}{en}\mathcal{K}(n) + T_e\mathcal{K}(\phi) - T_e\nabla\cdot\left(v_{\parallel e}\mathbf{b}\right) + 0.71\frac{T_e}{en}\nabla\cdot\left(j_\parallel\mathbf{b}\right) \\ &+ \frac{0.51 m_e}{e^2\tau_{en}}\frac{j_\parallel^2}{n} + \frac{1}{n}\nabla\cdot\left(3.16\frac{nT_e\tau_{en}}{m_e}\nabla_\parallel T_e\right) + \frac{3}{2}\mathcal{D}_{T_e}(T_e) + \frac{3}{2}S_{T_e},\end{aligned} \tag{A.27}$$

$$\nabla_\perp^2 A_\parallel = -\mu_0 j_\parallel. \tag{A.28}$$

where the $E \times B$ advective derivative and curvature operator are defined as:

$$\frac{d}{dt} := \frac{\partial}{\partial t} + \left(\frac{\mathbf{B}}{B^2}\times\nabla\phi\right)\cdot\nabla,$$

$$\mathcal{K}(f) := -\left(\nabla\times\frac{\mathbf{B}}{B^2}\right)\cdot\nabla f.$$

Equations (A.23-A.28) represent the continuity equation, vorticity (quasineutrality) equation, parallel momentum balance, Ohm's law with electromagnetic induction and electron inertia, electron temperature equation and Ampere's law. For this study we use the electron-neutral collision time τ_{en} in the resistivity and heat-conductivity coefficients.

For numerical stability, several kinds of diffusion are applied to the system, represented by the operator $\mathcal{D}_f = \nu_{f\perp}\nabla_\perp^6 f + \nu_{f\parallel}\nabla\cdot\left(\mathbf{b}\nabla_\parallel f\right) + \nabla\cdot\left(\nu_{f,\mathrm{buffer}}\nabla_\perp f\right)$. Within a poloidal plane, a 6^{th} order hyperdiffusion with a small prefactor is applied on all quantities to prevent energy from accumulating at grid scale – since the physical turbulence dissipation scale is expected to be too small to resolve. A parallel diffusion, with a small prefactor, is applied to the density, parallel velocity and vorticity to stabilise the parallel centred-difference scheme. Finally, in order to prevent spurious $E \times B$ influxes of heat and particles due to electric fields along the perpendicular boundaries, a diffusion is applied on all quantities except the potential near the boundaries of the limiting flux surfaces (but not in front of the targets).

The particle and temperature sources, S_n and S_{Te} respectively, have the shape given in section 2.5. The source rates were tuned to match the nominal parameters, giving a particle source rate of 2.18×10^{18} s^{-1} and a power source rate of 8.83 W. Additionally, to prevent the equations from becoming stiff due to low values of density and temperature, an adaptive source was used to prevent the density from dropping below 5×10^{-15} m^{-3} and the temperature below 2.21 eV.

A penalization technique is used for the implementation of boundary conditions [33] at the targets. A drift corrected Bohm-Chodura boundary condition with a flow-reversal limit is used:

$$u_\parallel \hat{\mathbf{b}} + \mathbf{u}_{E\times B} \cdot \hat{\mathbf{n}} = \max\left(c_s \hat{\mathbf{b}}, u_{\parallel,upstream} \hat{\mathbf{b}}, 0\right), \tag{A.29}$$

for the magnetic field line pointing onto the target. In the absence of local $E \times B$ drifts, the parallel velocity is simply forced to the greater of the local sound speed or the parallel velocity at its 'upstream' neighbour. However, when there is an $E \times B$ drift across the boundary, the parallel velocity is adapted to compensate for the spurious heat and particle influx up to the point that the parallel velocity would point into the domain. Due to the very low angle of incidence in TORPEX (between 0.5° to 1.2°), the drift-correction is outside the range of validity ($\geq 1.3°$ [77]), and the resulting flows are highly supersonic. The boundary condition is used nevertheless, since it is close to being valid and preventing spurious influxes is highly desirable.

Furthermore, insulating sheath boundary conditions $\phi = \Lambda T_e$, $j_\parallel = 0$, the 'sheath heat transmission' boundary condition $\nabla_\parallel T_e = -\gamma_e \left(\chi_{\parallel e0} T_e^{5/2}\right)^{-1} T_e n u_\parallel$ for $\gamma_e = 2.5$, and simple upwinding for density and vorticity – whereby we set the boundary value to the nearest interior upstream neighbour – is used. At the outer limiting flux surfaces of the simulation domain we use a simple set of boundary conditions, since they have less impact than the parallel boundary conditions. For this study we use $\partial_w n = 0$, $\partial_w T_e = 0$, $\phi = \Lambda T_e$, $\omega = 0$, $\partial_w u_\parallel = 0$, $j_\parallel = 0$, where ∂_w is the directional derivative to the limiting flux surfaces.

A.4 STORM

The variant of STORM used for this project implements a cold-ion, electrostatic, drift-reduced set of equations, similar to [37] but with some modifications, described below, to very approximately take into account the large background density of neutral gas in TORPEX. STORM is implemented in the BOUT++ framework [78, 79] (using a development version of the 4.4 series [80]) and uses a flux surface aligned grid and field-aligned parallel derivatives.

The equations evolved are,

$$
\begin{aligned}
\frac{\partial n}{\partial t} &= -v_{e\|}\nabla_{\|}n - \frac{1}{B}\mathbf{b}\times\nabla\phi\cdot\nabla n - nB\nabla_{\|}\left(\frac{v_{e\|}}{B}\right) \\
&\quad + \frac{1}{e}\nabla\times\left(\frac{\mathbf{b}}{B}\right)\cdot\nabla p_e - n\nabla\times\left(\frac{\mathbf{b}}{B}\right)\cdot\nabla\phi + S_n + \nabla_{\perp}\left(D_{\perp}\nabla_{\perp}n\right), \qquad \text{(A.30)} \\
\frac{\partial v_{i\|}}{\partial t} &= -v_{i\|}\nabla_{\|}v_{i\|} - \frac{1}{B}\mathbf{b}\times\nabla\phi\cdot\nabla v_{i\|} \\
&\quad - \frac{e}{m_i}\nabla_{\|}\phi + \frac{R_{i\|}}{m_i n} - \frac{v_{i\|}S_n}{n}, \qquad \text{(A.31)} \\
\frac{\partial v_{e\|}}{\partial t} &= -v_{e\|}\nabla_{\|}v_{e\|} - \frac{1}{B}\mathbf{b}\times\nabla\phi\cdot\nabla v_{e\|} - \frac{\nabla_{\|}p_e}{m_e n} \\
&\quad + \frac{e}{m_e}\nabla_{\|}\phi + \frac{R_{e\|}}{m_e n} - \frac{v_{e\|}S_n}{n}, \qquad \text{(A.32)} \\
\frac{\partial \omega}{\partial t} &= -\frac{1}{B}\mathbf{b}\times\nabla\phi\cdot\nabla\omega - v_{i\|}\nabla_{\|}\omega + B\nabla_{\|}\left(\frac{j_{\|}}{B}\right) \\
&\quad + \nabla\times\left(\frac{\mathbf{b}}{B}\right)\cdot\nabla p_e + \nabla\cdot\left(\mu_{\omega}\nabla_{\perp}\omega\right), \qquad \text{(A.33)} \\
\frac{\partial T_e}{\partial t} &= -v_{e\|}\nabla_{\|}T_e - \frac{1}{B}\mathbf{b}\times\nabla\phi\cdot\nabla T_e - \frac{2B}{3n}\nabla_{\|}\left(\frac{q_{e\|}}{B}\right) \\
&\quad + \frac{2T_e}{3en}\nabla\times\left(\frac{\mathbf{b}}{B}\right)\cdot\left(\nabla p_e - en\nabla\phi + \frac{5}{2}n\nabla T_e\right) \\
&\quad - \frac{2T_e}{3}B\nabla_{\|}\left(\frac{v_{e\|}}{B}\right) + \frac{2}{3}\frac{\left(v_{i\|} - v_{e\|}\right)}{n}R_{ei\|} \\
&\quad + \frac{2S_E}{3n} + \frac{v_{e\|}^2 S_n}{3m_e n} - \frac{T_e S_n}{n} + \frac{2}{3n}\nabla\cdot\left(\kappa_{e\perp}\nabla_{\perp}T_e\right). \qquad \text{(A.34)}
\end{aligned}
$$

Parallel and perpendicular (subscript $\|$ and $\perp$) are relative to the fixed background magnetic field, whose magnitude and direction are B and $\mathbf{b}$. The proton charge is e, the ion and electron masses m_i and m_e. The sources of density S_n and energy S_E have the shape given in Section 2.2; their amplitudes were adjusted to match nominal values of $n = 2.1\times10^{16}$ m^{-3} and $T_e = 5.3$ eV at $R = 0.96$ m, Z =0. The resulting prefactors were 2.36×10^{20} s^{-1}m^{-3} for the particle source and 426 Wm^{-3} for the energy source. For this study we use constant perpendicular dissipation coefficients for particle diffusion $D_{\perp} = 0.522$ m^2 s^{-1}, perpendicular viscosity $\mu_{\omega} = 0.522$ m^2 s^{-1}, and perpendicular thermal conductivity $\kappa_{e\perp} = 5.22\times10^{15}$ m^{-1}s^{-1}. The generalised vorticity is related to the electrostatic potential ϕ as $\omega = \nabla\cdot\left(\left(n_0/B^2\right)\nabla_{\perp}\phi\right)$, and uses a form of Boussinesq approximation to replace n with a constant reference density $n_0 = 10^{16}$ m^{-3}.

Allowance for the background of molecular hydrogen is made by adding an extra term to the parallel friction terms $R_{e\|}$, $R_{i\|}$ and modifying the collision frequency in the electron parallel thermal conduction $q_{e\|}$. The electron-molecule collision frequency is estimated as follows. The momentum transfer cross-section for electrons impacting molecular hydrogen is $\sigma_{eH_2} \approx 10^{-19}$ m^{-2} for electron energies in the range 5−10 eV [51]. The molecular pressure is taken to be 0.02 Pa at 298.15 K, giving a molecular density $n_{H_2} \approx 4.9\times10^{18}$ m^{-3} using the ideal gas law. Finally estimating the electron velocity with the thermal speed at 5 eV, the electron-molecule collision frequency is $\nu_{eH_2} \approx n_{H_2}\sigma_{eH_2}v_{Te} \approx 6.5\times10^5$ s^{-1} $\approx 0.09\Omega_{ci}$, where the ion gyrofrequency is $\Omega_{ci} = eB/m_i$. To the electron-ion parallel friction $R_{ei\|} = 0.51m_e n_e\left(v_{i\|} - v_{e\|}\right)/\tau_{ei} - 0.71n_e\nabla_{\|}T_e$, where τ_{ei} is the usual electron-ion Coulomb collision time, we add a friction with stationary neutrals $R_{eH_2\|} = -m_e n v_{e\|}\nu_{eH_2}$, so

$R_{e\|} = R_{ei\|} + R_{eH_2\|}$ in the electron velocity equation. We also add a friction between ions and molecules $R_{iH_2\|} = -m_i n V_{i\|}\sqrt{m_e/m_i}\nu_{eH_2}$ to help stabilise parallel flows, so $R_{i\|} = -R_{ei\|} + R_{iH_2\|}$. The parallel thermal conduction coefficient was reduced from the value for electron-plasma collisions by a factor of $\nu_{ei}(T_e = 10\text{eV})/\nu_{eH_2} \approx 49.7$, while keeping the density and temperature dependence unchanged $q_{e\|} = -49.7 \times 3.16 n T_e \tau_{ei} \nabla_\| T_e/m_e - 0.71 n T_e \left(V_{i\|} - V_{e\|}\right)$. This form was found to be more numerically stable than attempts to alter the density or temperature dependence to better represent collisions with a constant-density background of stationary molecules.

At the parallel boundaries, STORM applies Bohm boundary conditions [81]. Due to the very shallow angle of the magnetic field to the wall in this TORPEX scenario, here we add an $E \times B$ drift correction to the ion parallel velocity boundary condition [82]. The expressions used are

$$v_{i\|,sh} = \pm\left[\left(\frac{T_e}{m_i + m_e}\right)^{1/2} - \frac{\mathbf{n}\cdot\mathbf{b}\times\nabla\phi}{B\sin\theta}\right], \tag{A.35}$$

$$v_{e\|,sh} = \pm\left(\frac{m_i T_e}{2\pi m_e\left(m_e + m_i\right)}\right)^{1/2}\exp\left(-e\phi/T_e\right), \tag{A.36}$$

$$q_{e\|,sh} = \pm\left[\left(\frac{1}{2}\ln\left(m_i/2\pi m_e\right) - \frac{1}{2}\right) n T_e v_{e\|,sh} - \frac{1}{2} m_e n v_{e\|,sh}^3\right] \tag{A.37}$$

where $\mathbf{n}$ is the outward pointing normal to the wall and θ is the angle between the magnetic field $\mathbf{b}$ and the wall. At the radial boundaries ϕ has a Dirichlet boundary condition set to a value that relaxes so that the time- and toroidally-averaged component of ϕ has zero gradient at the boundary. We apply Neumann radial boundary conditions to all other variables.

When solving $\omega = \nabla\cdot\left(\left(n_0/B^2\right)\nabla_\perp\phi\right)$ for the electrostatic potential, the equation is decomposed toroidally into Fourier modes and solved as a decoupled set of 1D radial ODEs for mode numbers $n > 0$ by neglecting parallel derivative terms using the assumption $k_\| \ll k_\perp$. Since this assumption does not hold for low-n modes and given the importance of axisymmetric $E \times B$ flows in the very shallow field line angles of the considered TORPEX scenario, the $n = 0$ mode is solved in 2D with an iterative scheme implemented via PETSc [83, 84, 85] and using the BoomerAMG algebraic multigrid preconditioner from Hypre [86, 87].

To improve numerical stability we introduce artificial source terms to impose a soft lower limit on the density of $n \gtrsim 5\times10^{14}$ m^{-3} and on the potential of $\phi \gtrsim 1$ V.

The grid size was 96 points in the direction perpendicular to flux surfaces, 128 points in the parallel direction and 64 points in the toroidal direction. Differential operators are discretized in the radial and parallel directions using second order finite differences, an Arakawa bracket [88] is used for the $E \times B$ advection terms, and toroidal derivatives are calculated using the FFT method. Parallel derivatives are calculated by transforming to a field-aligned grid using FFT interpolation in the toroidal direction, applying the finite-difference stencil, and transforming the result back with a second FFT interpolation in the toroidal direction. Ion and electron parallel velocities and the parallel heat flux are calculated on a staggered grid to avoid the chequerboard instability. Time integration uses the method of lines, and is solved using CVODE from the SUNDIALS suite [89].

STORM, employing standard BOUT++ grid geometry, uses the poloidal coordinate as the field-line coordinate. The very shallow field line pitch in TORPEX, in contrast to standard tokamaks, is unfavourable for this method as the parallel grid spacing $\Delta_\| = \Delta_\theta B/B_p$ is so much larger than the poloidal grid spacing Δ_θ, where B_p is the magnitude of the poloidal magnetic field. Although the poloidal grid spacing was adjusted to keep the parallel distance between grid points fairly constant over as much of the domain as possible, the parallel grid spacing nevertheless exceeded 2 m in the region within ~ 4 cm of the X-point. While this spacing is a small fraction of the parallel connection length of these field lines, which exceeds 100 m near the X-point, the effect of such a large parallel grid spacing is uncertain. Simulations with double the number of parallel grid points were numerically unstable, so a convergence check was performed by running simulations with half the number of parallel grid points. The lower resolution simulations were qualitatively similar to those presented in this paper, although with lower fluctuation amplitudes near the X-point, in the region with the worst parallel resolution.

References

[1] T. Eich, A.W. Leonard, R.A. Pitts, W. Fundamenski, R.J. Goldston, T.K. Gray, A. Herrmann, A. Kirk, A. Kallenbach, O. Kardaun, et al. Scaling of the tokamak near the scrape-off layer h-mode power width and implications for iter. *Nuclear Fusion*, 53(9):093031, 2013.

[2] M. Wischmeier. High density operation for reactor-relevant power exhaust. *Journal of Nuclear Materials*, 463:22 – 29, 2015. PLASMA-SURFACE INTERACTIONS 21.

[3] D. Brunner, B. LaBombard, A.Q. Kuang, and J.L. Terry. High-resolution heat flux width measurements at reactor-level magnetic fields and observation of a unified width scaling across confinement regimes in the alcator c-mod tokamak. *Nuclear Fusion*, 58(9):094002, jul 2018.

[4] R.A. Pitts, X. Bonnin, F. Escourbiac, H. Frerichs, J.P. Gunn, T. Hirai, A.S. Kukushkin, E. Kaveeva, M.A. Miller, D. Moulton, et al. Physics basis for the first iter tungsten divertor. *Nuclear Materials and Energy*, 20:100696, 2019.

[5] C S Pitcher and P C Stangeby. Experimental divertor physics. *Plasma Physics and Controlled Fusion*, 39(6):779–930, jun 1997.

[6] F. Wagner, G. Becker, K. Behringer, D. Campbell, A. Eberhagen, W. Engelhardt, G. Fussmann, O. Gehre, J. Gernhardt, G. v. Gierke, et al. Regime of improved confinement and high beta in neutral-beam-heated divertor discharges of the asdex tokamak. *Phys. Rev. Lett.*, 49:1408–1412, Nov 1982.

[7] T.D. Rognlien, G.D. Porter, and D.D. Ryutov. Influence of exb and grad-b drift terms in 2-d edge/sol transport simulations. *Journal of Nuclear Materials*, 266–269:654 – 659, 1999.

[8] D. Galassi, P. Tamain, H. Bufferand, G. Ciraolo, Ph. Ghendrih, C. Baudoin, C. Colin, N. Fedorczak, N. Nace, and E. Serre. Drive of parallel flows by turbulence and large-scale e x b transverse transport in divertor geometry. *Nuclear Fusion*, 57(3):036029, 2017.

[9] Paola Paruta, P. Ricci, F. Riva, C. Wersal, C. Beadle, and B. Frei. Simulation of plasma turbulence in the periphery of diverted tokamak by using the gbs code. *Physics of Plasmas*, 25(11):112301, 2018.

[10] S. I. Krasheninnikov, D. A. D'Ippolito, and J. R. Myra. Recent theoretical progress in understanding coherent structures in edge and sol turbulence. *Journal of Plasma Physics*, 74(5):679–717, 2008.

[11] D. A. D'Ippolito, J. R. Myra, and S. J. Zweben. Convective transport by intermittent blob-filaments: Comparison of theory and experiment. *Physics of Plasmas*, 18(6):060501, 2011.

[12] J.L. Terry, S.J. Zweben, M.V. Umansky, I. Cziegler, O. Grulke, B. LaBombard, and D.P. Stotler. Spatial structure of scrape-off-layer filaments near the midplane and x-point regions of alcator-c-mod. *Journal of Nuclear Materials*, 390-391:339 – 342, 2009. Proceedings of the 18th International Conference on Plasma-Surface Interactions in Controlled Fusion Device.

[13] N.R. Walkden, J. Harrison, S.A. Silburn, T. Farley, S.S. Henderson, A. Kirk, F. Militello, and A. Thornton and. Quiescence near the x-point of MAST measured by high speed visible imaging. *Nuclear Fusion*, 57(12):126028, sep 2017.

[14] R D Nem, P Manz, J Juul Rasmussen, N Vianello, N Walkden, V Naulin, B Sieglin, A Herrmann, and D Brida. Quiescent regions below the x-point in ASDEX upgrade. *Plasma Physics and Controlled Fusion*, 63(6):065005, apr 2021.

[15] J.R. Harrison, G.M. Fishpool, and B.D. Dudson. Filamentary transport in the private flux region in MAST. *Journal of Nuclear Materials*, 463:757 – 760, 2015. PLASMA-SURFACE INTERACTIONS 21Proceedings of the 21st International Conference on Plasma-Surface Interactions in Controlled Fusion Devices Kanazawa, Japan May 26-30, 2014.

[16] F. Nespoli, P. Tamain, N. Fedorczak, G. Ciraolo, D. Galassi, R. Tatali, E. Serre, Y. Marandet, H. Bufferand, and Ph. Ghendrih. 3d structure and dynamics of filaments in turbulence simulations of WEST diverted plasmas. *Nuclear Fusion*, 59(9):096006, jul 2019.

[17] Ammar H. Hakim, Noah R. Mandell, T. N. Bernard, M. Francisquez, G. W. Hammett, and E. L. Shi. Continuum electromagnetic gyrokinetic simulations of turbulence in the tokamak scrape-off layer and laboratory devices. *Physics of Plasmas*, 27(4):042304, 2020.

[18] C. S. Chang, S. Ku, G. R. Tynan, R. Hager, R. M. Churchill, I. Cziegler, M. Greenwald, A. E. Hubbard, and J. W. Hughes. Fast low-to-high confinement mode bifurcation dynamics in a tokamak edge plasma gyrokinetic simulation. *Phys. Rev. Lett.*, 118:175001, Apr 2017.

[19] F.D. Halpern and P. Ricci. Velocity shear, turbulent saturation, and steep plasma gradients in the scrape-off layer of inner-wall limited tokamaks. *Nuclear Fusion*, 57(3):034001, 2017.

[20] R. Tatali, E. Serre, P. Tamain, D. Galassi, P. Ghendrih, F. Nespoli, H. Bufferand, T. Cartier-Michaud, and G. Ciraolo. Impact of collisionality on turbulence in the edge of tokamak plasma using 3d global simulations. *Nuclear Fusion*, 61(5):056002, mar 2021.

[21] M. Giacomin and P. Ricci. Investigation of turbulent transport regimes in the tokamak edge by using two-fluid simulations. *Journal of Plasma Physics*, 86(5):905860502, 2020.

[22] P Ricci, C. Theiler, A. Fasoli, I. Furno, B. Labit, S. H. Müller, M. Podestà, and F. M. Poli. Langmuir probe-based observables for plasma-turbulence code validation and application to the torpex basic plasma physics experiment. *Phys. Plasmas*, 16:055703, 2009.

[23] Paolo Ricci, C. Theiler, A. Fasoli, I. Furno, K. Gustafson, D. Iraji, and J. Loizu. Methodology for turbulence code validation: Quantification of simulation-experiment agreement and application to the torpex experiment. *Physics of Plasmas*, 18(3):032109, 2011.

[24] S. Coda, M. Agostini, R. Albanese, S. Alberti, E. Alessi, S. Allan, J. Allcock, R. Ambrosino, H. Anand, Y Andrèbe, et al. Physics research on the TCV tokamak facility: from conventional to alternative scenarios and beyond. *Nuclear Fusion*, 59(11):112023, aug 2019.

[25] F Riva, CK Tsui, JA Boedo, P Ricci, and TCV Team. Shaping effects on scrape-off layer plasma turbulence: A rigorous validation of three-dimensional simulations against tcv measurements. *Physics of Plasmas*, 27(1):012301, 2020.

[26] F Riva, C Colin, J Denis, L Easy, I Furno, J Madsen, F Militello, V Naulin, A H Nielsen, J M B Olsen, J T Omotani, J J Rasmussen, P Ricci, E Serre, P Tamain, and C Theiler. Blob dynamics in the torpex experiment: a multi-code validation. *Plasma Physics and Controlled Fusion*, 58(4):044005, 2016.

[27] F Militello, N R Walkden, T Farley, W A Gracias, J Olsen, F Riva, L Easy, N Fedorczak, I Lupelli, J Madsen, A H Nielsen, P Ricci, P Tamain, and J Young. Multi-code analysis of scrape-off layer filament dynamics in mast. *Plasma Physics and Controlled Fusion*, 58(10):105002, 2016.

[28] B D Dudson, W A Gracias, R Jorge, A H Nielsen, J M B Olsen, P Ricci, C Silva, P Tamain, G Ciraolo, N Fedorczak, D Galassi, J Madsen, F Militello, N Nace, J J Rasmussen, F Riva, and E Serre. Edge turbulence in ISTTOK: a multi-code fluid validation. *Plasma Physics and Controlled Fusion*, 63(5):055013, apr 2021.

[29] A. Fasoli, B. Labit, M. McGrath, S. H. Müller, G. Plyushchev, M. Podestà, and F. M. Poli. Electrostatic turbulence and transport in a simple magnetized plasma. *Physics of Plasmas*, 13(5):055902, 2006.

[30] I. Furno, F. Avino, A. Bovet, A. Diallo, A. Fasoli, K. Gustafson, D. Iraji, B. Labit, J. Loizu, S. H. Müller, and et al. Plasma turbulence, suprathermal ion dynamics and code validation on the basic plasma physics device torpex. *Journal of Plasma Physics*, 81(3):345810301, 2015.

[31] A Fasoli, I Furno, and P Ricci. The role of basic plasmas studies in the quest for fusion power. *Nature Physics*, 15:872–875, 2019.

[32] Matthias Wiesenberger, Lukas Einkemmer, Markus Held, Albert Gutierrez-Milla, Xavier Sáez, and Roman Iakymchuk. Reproducibility, accuracy and performance of the feltor code and library on parallel computer architectures. *Computer Physics Communications*, 238:145 – 156, 2019.

[33] A. Stegmeir, A. Ross, T. Body, M. Francisquez, W. Zholobenko, D. Coster, O. Maj, P. Manz, F. Jenko, B. N. Rogers, and K. S. Kang. Global turbulence simulations of the tokamak edge region with grillix. *Physics of Plasmas*, 26(5):052517, 2019.

[34] L. Easy, F. Militello, J. Omotani, B. Dudson, E. Havlíčková, P. Tamain, V. Naulin, and A. H. Nielsen. Three dimensional simulations of plasma filaments in the scrape off layer: A comparison with models of reduced dimensionality. *Physics of Plasmas*, 21(12):122515, 2014.

[35] M Giacomin, LN Stenger, and P Ricci. Turbulence and flows in the plasma boundary of snowflake magnetic configurations. *Nuclear Fusion*, 60(2):024001, 2020.

[36] W Zholobenko, T Body, P Manz, A Stegmeir, B Zhu, M Griener, G D Conway, D Coster, and F Jenko. Electric field and turbulence in global braginskii simulations across the ASDEX upgrade edge and scrape-off layer. *Plasma Physics and Controlled Fusion*, 63(3):034001, feb 2021.

[37] Fabio Riva, Fulvio Militello, Sarah Elmore, John T Omotani, Ben Dudson, Nick R Walkden, and the MAST team. Three-dimensional plasma edge turbulence simulations of the mega ampere spherical tokamak and comparison with experimental measurements. *Plasma Physics and Controlled Fusion*, 61(9):095013, aug 2019.

[38] P. W. Terry, M. Greenwald, J.-N. Leboeuf, G. R. McKee, D. R. Mikkelsen, W. M. Nevins, D. E. Newman, D. P. Stotler, Task Group on Verification and Validation, U.S. Burning Plasma Organization, and U.S. Transport Task Force. Validation in fusion research: Towards guidelines and best practices. *Physics of Plasmas*, 15(6):062503, June 2008.

[39] M Podestà, A Fasoli, B Labit, M McGrath, S H Müller, and F M Poli. Plasma production by low-field side injection of electron cyclotron waves in a simple magnetized torus. *Plasma Physics and Controlled Fusion*, 47(11):1989–2002, oct 2005.

[40] S. H. Müller, A. Fasoli, B. Labit, M. McGrath, O. Pisaturo, G. Plyushchev, M. Podestà, and F. M. Poli. Basic turbulence studies on torpex and challenges in the theory-experiment comparison. *Physics of Plasmas*, 12(9):090906, 2005.

[41] M. Baquero-Ruiz, F. Avino, O. Chellai, A. Fasoli, I. Furno, R. Jacquier, F. Manke, and S. Patrick. Dual langmuir-probe array for 3d plasma studies in torpex. *Review of Scientific Instruments*, 87(11):113504, 2016.

[42] C. Theiler, J. Loizu, I. Furno, A. Fasoli, and P. Ricci. Properties of convective cells generated in magnetized toroidal plasmas. *Physics of Plasmas*, 19(8):082304, 2012.

[43] F. Avino, A. Fasoli, I. Furno, P. Ricci, and C. Theiler. x-point effect on plasma blob dynamics. *Phys. Rev. Lett.*, 116:105001, Mar 2016.

[44] H. Johnsen, H. L. Pécseli, and J. Trulsen. Conditional eddies in plasma turbulence. *The Physics of Fluids*, 30(7):2239–2254, 1987.

[45] I. Furno, B. Labit, A. Fasoli, F. M. Poli, P. Ricci, C. Theiler, S. Brunner, A. Diallo, J. P. Graves, M. Podestà, and S. H. Müller. Mechanism for blob generation in the torpex toroidal plasma. *Physics of Plasmas*, 15(5):055903, 2008.

[46] S. H. Müller, A. Diallo, A. Fasoli, I. Furno, B. Labit, and M. Podestà. Plasma blobs in a basic toroidal experiment: Origin, dynamics, and induced transport. *Physics of Plasmas*, 14(11):110704, 2007.

[47] C. Theiler, I. Furno, P. Ricci, A. Fasoli, B. Labit, S. H. Müller, and G. Plyushchev. Cross-field motion of plasma blobs in an open magnetic field line configuration. *Phys. Rev. Lett.*, 103:065001, Aug 2009.

[48] Paolo Ricci and B. N. Rogers. Turbulence phase space in simple magnetized toroidal plasmas. *Phys. Rev. Lett.*, 104:145001, Apr 2010.

[49] K. Rypdal, Å. Fredriksen, O. M. Olsen, and K. G. Hellblom. Microwave-plasma in a simple magnetized torus. *Physics of Plasmas*, 4(5):1468–1480, 1997.

[50] S. I. Braginskii. *Transport Processes in a Plasma*, volume 1. Provided by the SAO/NASA Astrophysics Data System, 1965.

[51] Jung-Sik Yoon, Young-Woo Kim, Deuk-Chul Kwon, Mi-Young Song, Won-Seok Chang, Chang-Geun Kim, Vijay Kumar, and BongJu Lee. Electron-impact cross sections for deuterated hydrogen and deuterium molecules. *Reports on Progress in Physics*, 73(11):116401, oct 2010.

[52] R.K. Janev, W.D. Langer, D.E. Post, and Evans K. *Electron Impact Collision Processes. In: Elementary Processes in Hydrogen-Helium Plasmas. Springer Series on Atoms+Plasmas, vol 4.* Springer, Berlin, Heidelberg, 1987.

[53] M. Wiesenberger, J. Madsen, and A. Kendl. Radial convection of finite ion temperature, high amplitude plasma blobs. *Physics of Plasmas*, 21(9):092301, 2014.

[54] M. Held, M. Wiesenberger, and A. Stegmeir. Three discontinuous galerkin schemes for the anisotropic heat conduction equation on non-aligned grids. *Computer Physics Communications*, 199:29–39, 2016.

[55] K. Bodi, G Ciraolo, Ph. Ghendrih, Schwander F., Serre E., and P. Tamain. Impact of the boussinesq approximation in tokamak scrape-off layer turbulence. In *Proceedings of 38th EPS conference on Plasma Physics*, 2011.

[56] Morales J., B Frei, F. Halpern, Musil F., Paruta P., P. Ricci, Riva F., Siffert M., and Wersal C. The impact of the boussinesq approximation on plasma turbulence in the scrape-off layer. In *Proceedings of 43th EPS conference on Plasma Physics*, 2016.

[57] M. Held, M. Wiesenberger, R. Kube, and A. Kendl. Non-oberbeck–boussinesq zonal flow generation. *Nuclear Fusion*, 58(10):104001, jul 2018.

[58] J. Loizu, P. Ricci, F. D. Halpern, and S. Jolliet. Boundary conditions for plasma fluid models at the magnetic presheath entrance. *Physics of Plasmas*, 19(12):122307, 2012.

[59] Ronald H. Cohen and Dmitri Ryutov. Drifts, boundary conditions and convection on open field lines. *Physics of Plasmas*, 6(5):1995–2001, 1999.

[60] A. Paredes, H. Bufferand, G. Ciraolo, F. Schwander, E. Serre, P. Ghendrih, and P. Tamain. A penalization technique to model plasma facing components in a tokamak with temperature variations. *Journal of Computational Physics*, 274:283 – 298, 2014.

[61] B Nold, G D Conway, T Happel, H W Müller, M Ramisch, V Rohde, U Stroth, and the ASDEX Upgrade Team. Generation of blobs and holes in the edge of the asdex upgrade tokamak. *Plasma Physics and Controlled Fusion*, 52(6):065005, 2010.

[62] SHANE A. RICHARDS. Completed richardson extrapolation in space and time. *Communications in Numerical Methods in Engineering*, 13(7):573–582, 1997.

[63] Fabio Riva, Paolo Ricci, Federico D. Halpern, Sébastien Jolliet, Joaquim Loizu, and Annamaria Mosetto. Verification methodology for plasma simulations and application to a scrape-off layer turbulence code. *Physics of Plasmas*, 21(6):062301, 2014.

[64] O. Février, C. Theiler, H. De Oliveira, B. Labit, N. Fedorczak, and A. Baillod. Analysis of wall-embedded langmuir probe signals in different conditions on the tokamak à configuration variable. *Review of Scientific Instruments*, 89(5):053502, 2018.

[65] P Ricci, F Riva, C Theiler, A Fasoli, I Furno, FD Halpern, and J Loizu. Approaching the investigation of plasma turbulence through a rigorous verification and validation procedure: A practical example. *Physics of Plasmas*, 22(5):055704, 2015.

[66] D. S. Oliveira, T. Body, D. Galassi, C. Theiler, E. Laribi, P. Tamain, A. Stegmeir, M. Giacomin, W. Zholobenko, P. Ricci, et al. Validation of edge turbulence codes against the tcv-x21 diverted l-mode reference case. *Submitted to Nuclear Fusion*, 2021.

[67] M. Giacomin, P. Ricci, A. Coroado, G. Fourestey, D. Galassi, E. Lanti, D. Mancini, N. Richart, L. N. Stenger, and N. Varini. The gbs code for the self-consistent simulation of plasma turbulence and kinetic neutral dynamics in the tokamak boundary. *Journal of Computational Physics*, Submitted, 2021.

[68] M. Wiesenberger. *Gyrofluid computations of filament dynamics in tokamak scrape-off layers*. PhD thesis, University of Innsbruck, 2014.

[69] M. Held. *Full-F gyro-fluid modelling of the tokamak edge and scrape-off layer*. PhD thesis, University of Innsbruck, 2016.

[70] J. Madsen. Full-f gyrofluid model. *Phys. Plasmas*, 20:072301, 2013.

[71] Matthias Wiesenberger and Markus Held. Angular momentum and rotational energy of mean flows in toroidal magnetic fields. *Nuclear Fusion*, 60(9):096018, 2020.

[72] M. Held, M. Wiesenberger, and A. Kendl. Padé-based arbitrary wavelength polarization closures for full-f gyrokinetic and -fluid models. *Nuclear Fusion*, 60:066014, 2020.

[73] A. J. Cerfon and J. P. Freidberg. ”one size fits all” analytic solutions to the grad-shafranov equation. *Phys. Plasmas*, 17(3):032502, 2010.

[74] P Ricci, F D Halpern, S Jolliet, J Loizu, A Mosetto, A Fasoli, I Furno, and C Theiler. Simulation of plasma turbulence in scrape-off layer conditions: the gbs code, simulation results and code validation. *Plasma Physics and Controlled Fusion*, 54(12):124047, 2012.

[75] G. Q. Yu, S. I. Krasheninnikov, and P. N. Guzdar. Two-dimensional modelling of blob dynamics in tokamak edge plasmas. *Phys. Plasmas*, 13(4):042508, 2006.

[76] Andreas Stegmeir, David Coster, Alexander Ross, Omar Maj, Karl Lackner, and Emanuele Poli. GRILLIX: a 3d turbulence code based on the flux-coordinate independent approach. *Plasma Physics and Controlled Fusion*, 60(3):035005, jan 2018.

[77] Ronald H. Cohen and Dmitri D. Ryutov. Plasma sheath in a tilted magnetic field: Closing of the diamagnetic currents; effect on plasma convection. *Physics of Plasmas*, 2(6):2011–2019, Jun 1995.

[78] B.D. Dudson, M.V. Umansky, X.Q. Xu, P.B. Snyder, and H.R. Wilson. BOUT++: A framework for parallel plasma fluid simulations. *Computer Physics Communications*, 180(9):1467–1480, sep 2009.

[79] B. D. Dudson, J. Madsen, J. Omotani, P. Hill, L. Easy, and M. Løiten. Verification of BOUT++ by the method of manufactured solutions. *Physics of Plasmas*, 23(6):062303, 2016.

[80] Benjamin Daniel Dudson, Peter Alec Hill, David Dickinson, Joseph Parker, Adam Dempsey, Andrew Allen, Arka Bokshi, Brendan Shanahan, Brett Friedman, Chenhao Ma, David Schwörer, Dmitry Meyerson, Eric Grinaker, George Breyiannia, Hasan Muhammed, Haruki Seto, Hong Zhang, Ilon Joseph, Jarrod Leddy, Jed Brown, Jens Madsen, John Omotani, Joshua Sauppe, Kevin Savage, Licheng Wang, Luke Easy, Marta Estarellas, Matt Thomas, Maxim Umansky, Michael Løiten, Minwoo Kim, M Leconte, Nicholas Walkden, Olivier Izacard, Pengwei Xi, Peter Naylor, Fabio Riva, Sanat Tiwari, Sean Farley, Simon Myers, Tianyang Xia, Tongnyeol Rhee, Xiang Liu, Xueqiao Xu, and Zhanhui Wang. BOUT++, https://github.com/boutproject/BOUT-dev, 2020.

[81] P. C. Stangeby. *The Plasma Boundary of Magnetic Fusion Devices*. Bristol: Institute of Physics Publishing, 2000.

[82] P. C. Stangeby and A. V. Chankin. The ion velocity (bohm–chodura) boundary condition at the entrance to the magnetic presheath in the presence of diamagnetic and $E \times B$ drifts in the scrape-off layer. *Physics of Plasmas*, 2(3):707–715, 1995.

[83] Satish Balay, Shrirang Abhyankar, Mark F. Adams, Jed Brown, Peter Brune, Kris Buschelman, Lisandro Dalcin, Alp Dener, Victor Eijkhout, William D. Gropp, Dmitry Karpeyev, Dinesh Kaushik, Matthew G. Knepley, Dave A. May, Lois Curfman McInnes, Richard Tran Mills, Todd Munson, Karl Rupp, Patrick Sanan, Barry F. Smith, Stefano Zampini, Hong Zhang, and Hong Zhang. PETSc Web page. `https://www.mcs.anl.gov/petsc`, 2019.

[84] Satish Balay, Shrirang Abhyankar, Mark F. Adams, Jed Brown, Peter Brune, Kris Buschelman, Lisandro Dalcin, Alp Dener, Victor Eijkhout, William D. Gropp, Dmitry Karpeyev, Dinesh Kaushik, Matthew G. Knepley, Dave A. May, Lois Curfman McInnes, Richard Tran Mills, Todd Munson, Karl Rupp, Patrick Sanan, Barry F. Smith, Stefano Zampini, Hong Zhang, and Hong Zhang. PETSc users manual. Technical Report ANL-95/11 - Revision 3.14, Argonne National Laboratory, 2020.

[85] Satish Balay, William D. Gropp, Lois Curfman McInnes, and Barry F. Smith. Efficient management of parallelism in object oriented numerical software libraries. In E. Arge, A. M. Bruaset, and H. P. Langtangen, editors, *Modern Software Tools in Scientific Computing*, pages 163–202. Birkhäuser Press, 1997.

[86] Robert D. Falgout, Jim E. Jones, and Ulrike Meier Yang. The design and implementation of hypre, a library of parallel high performance preconditioners. In Are Magnus Bruaset and Aslak Tveito, editors, *Numerical Solution of Partial Differential Equations on Parallel Computers*, pages 267–294, Berlin, Heidelberg, 2006. Springer Berlin Heidelberg.

[87] Van Emden Henson and Ulrike Meier Yang. Boomeramg: A parallel algebraic multigrid solver and preconditioner. *Applied Numerical Mathematics*, 41(1):155–177, 2002. Developments and Trends in Iterative Methods for Large Systems of Equations - in memorium Rudiger Weiss.

[88] Akio Arakawa. Computational design for long-term numerical integration of the equations of fluid motion: Two-dimensional incompressible flow. part i. *Journal of Computational Physics*, 1(1):119–143, 1966.

[89] Alan C Hindmarsh, Peter N Brown, Keith E Grant, Steven L Lee, Radu Serban, Dan E Shumaker, and Carol S Woodward. SUNDIALS: Suite of nonlinear and differential/algebraic equation solvers. *ACM Transactions on Mathematical Software (TOMS)*, 31(3):363–396, 2005.

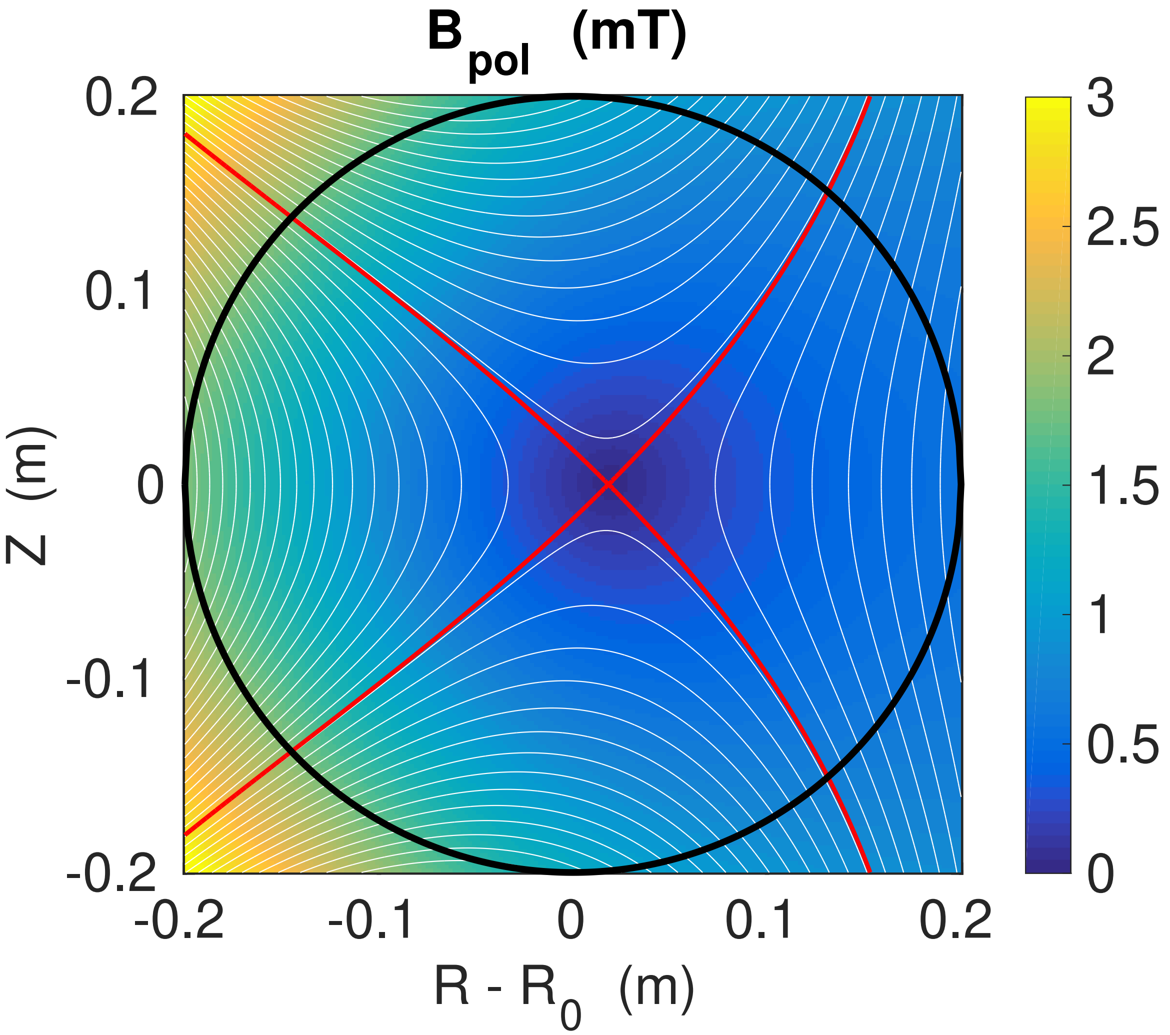
B_{pol} (mT)
0.2
0.1
0
-0.1
-0.2
Z (m)
-0.2
-0.1
0
0.1
0.2
$R - R_0$ (m)
3
2.5
2
1.5
1
0.5
0

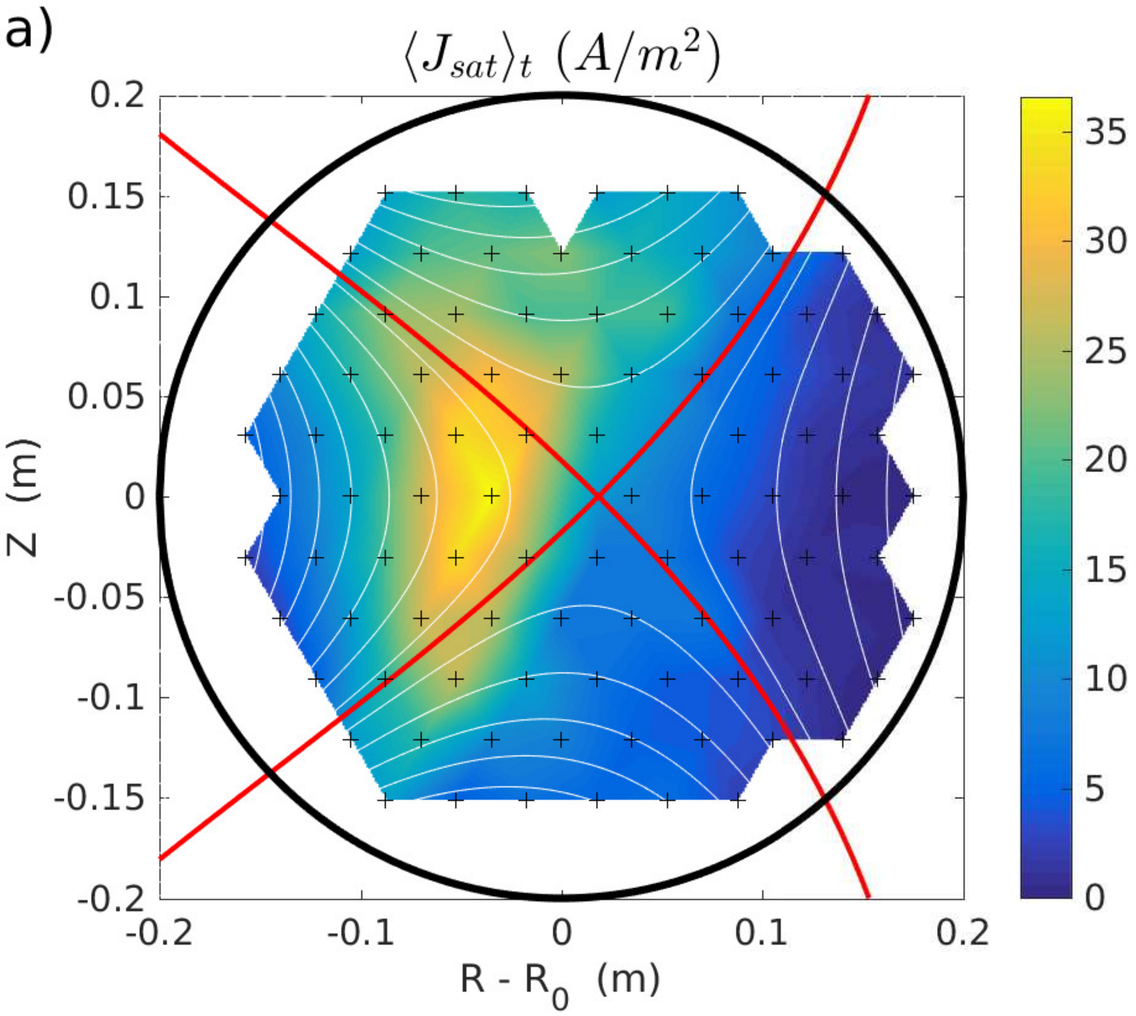
a)
$\langle J_{sat}\rangle_t$ (A/m^2)
0.2
0.15
0.1
0.05
0
-0.05
-0.1
-0.15
-0.2
Z (m)
-0.2
-0.1
0
0.1
0.2
R - R_0 (m)
35
30
25
20
15
10
5
0

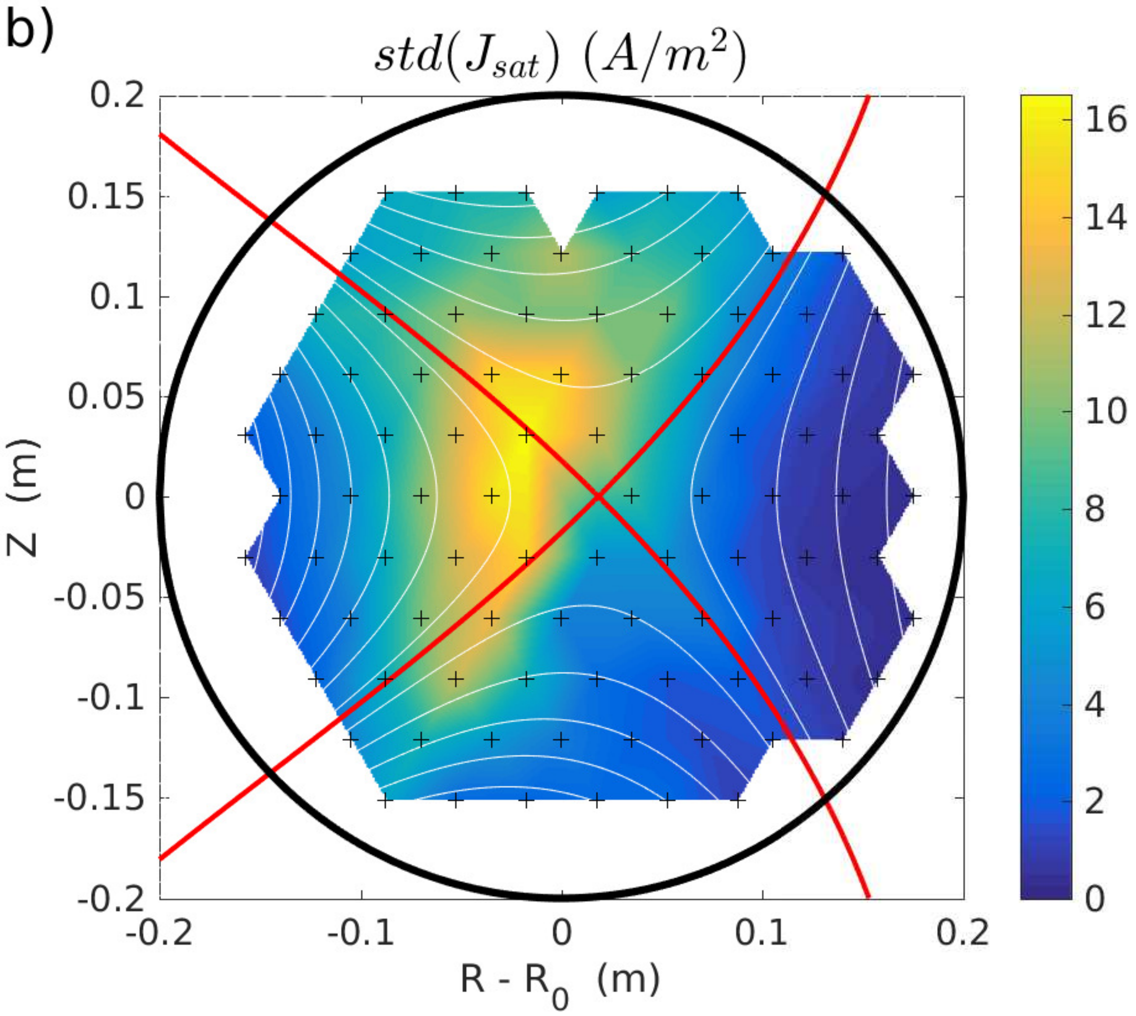
b)
$std(J_{sat})$ (A/m^2)
0.2
0.15
0.1
0.05
0
-0.05
-0.1
-0.15
-0.2
Z (m)
-0.2
-0.1
0
0.1
0.2
R - R_0 (m)
16
14
12
10
8
6
4
2
0

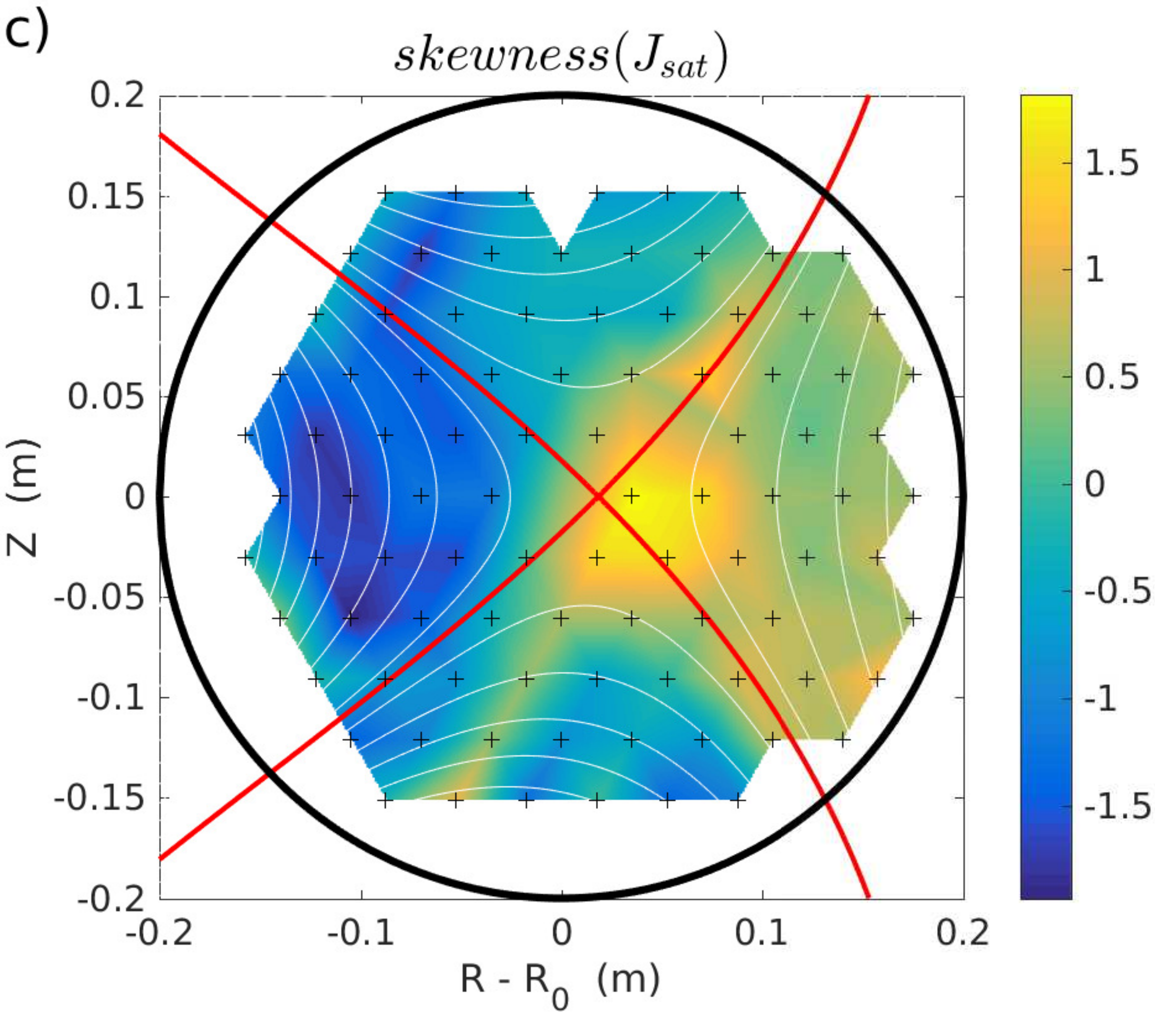
c)
$skewness(J_{sat})$
0.2
0.15
0.1
0.05
0
-0.05
-0.1
-0.15
-0.2
Z (m)
-0.2
-0.1
0
0.1
0.2
R - R_0 (m)
1.5
1
0.5
0
-0.5
-1
-1.5

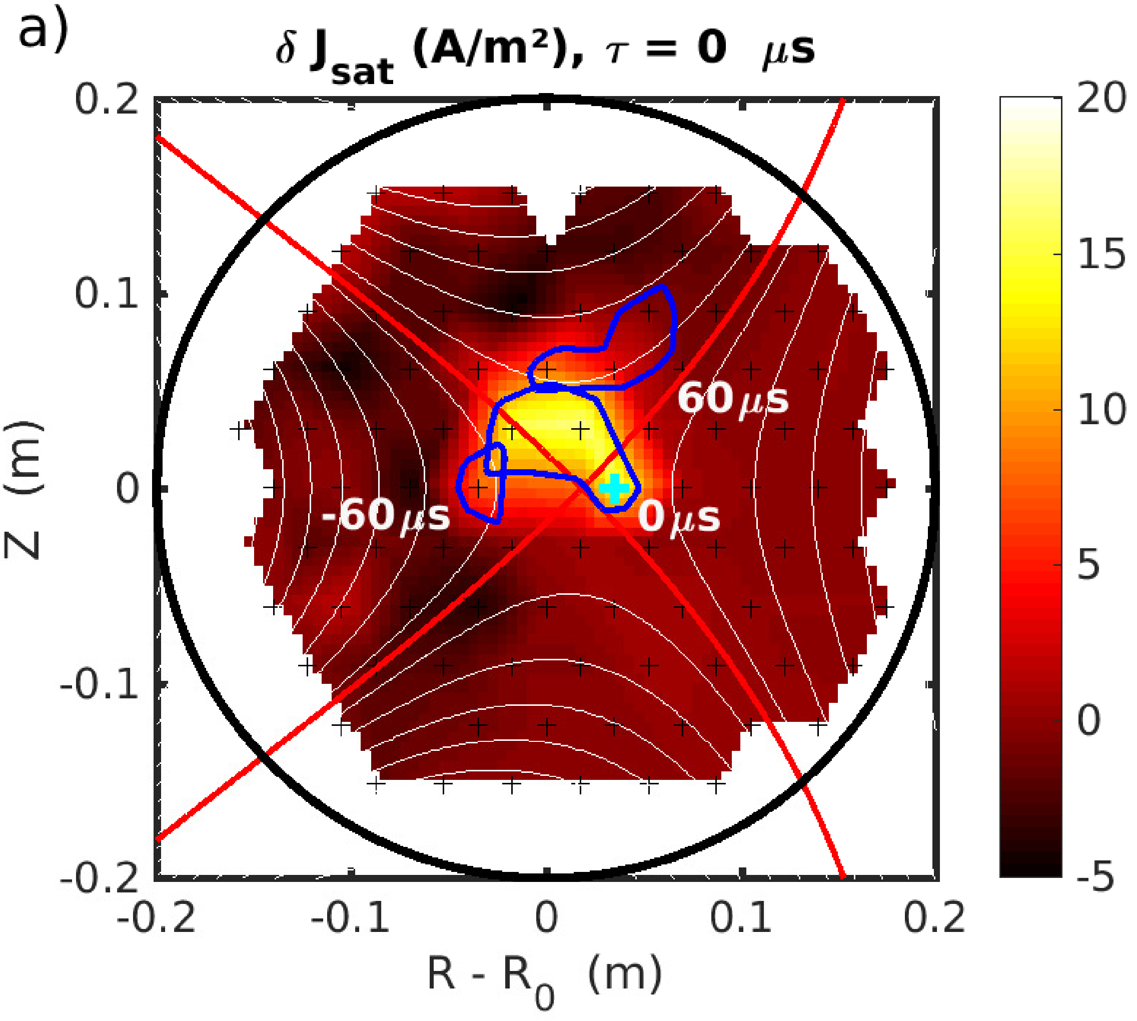
a)
δ J_sat (A/m²), τ = 0 μs
60 μs
-60 μs
0 μs
0.2
0.1
0
-0.1
-0.2
Z (m)
-0.2
-0.1
0
0.1
0.2
R - R_0 (m)
20
15
10
5
0
-5

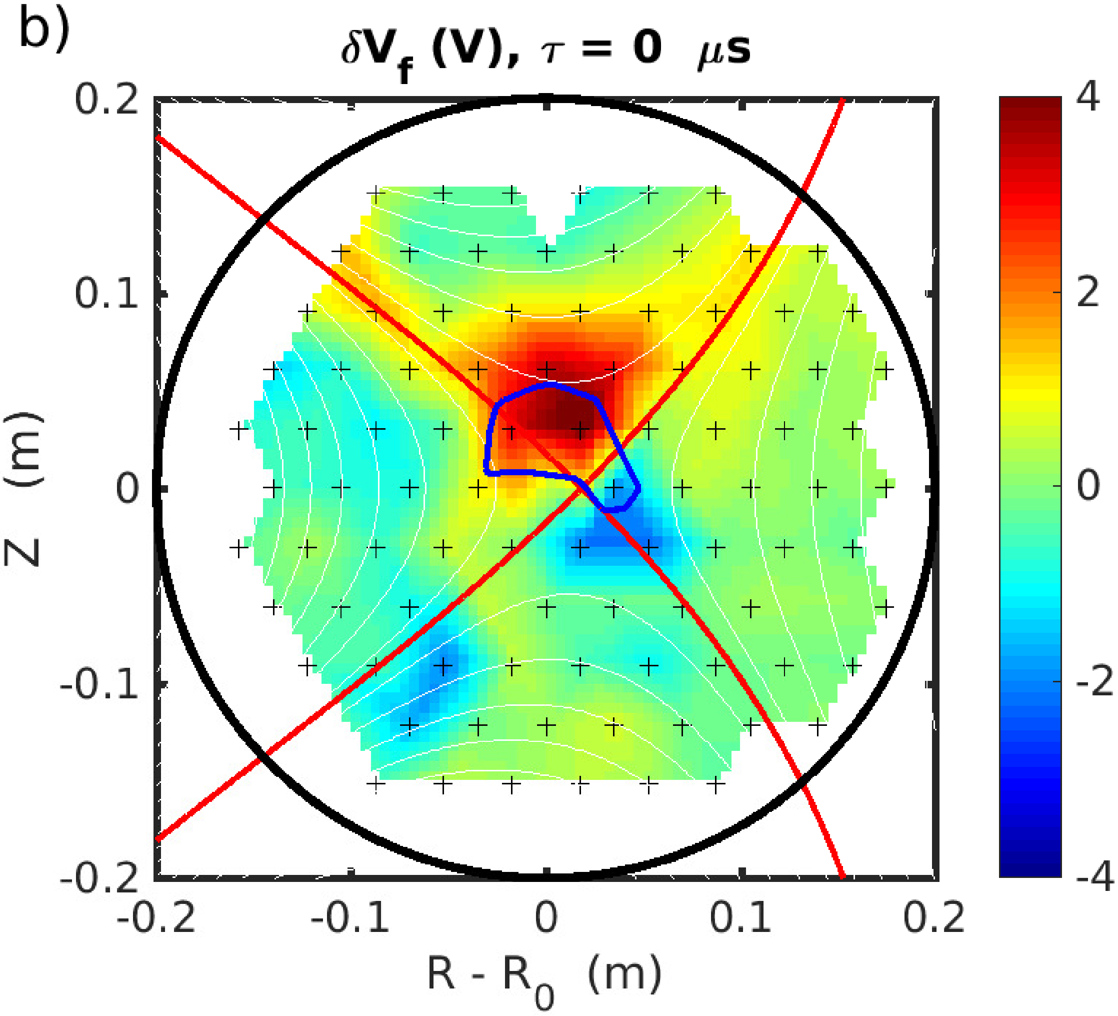
b)
δV_f (V), τ = 0 μs
0.2
0.1
0
-0.1
-0.2
Z (m)
-0.2
-0.1
0
0.1
0.2
R - R_0 (m)
4
2
0
-2
-4

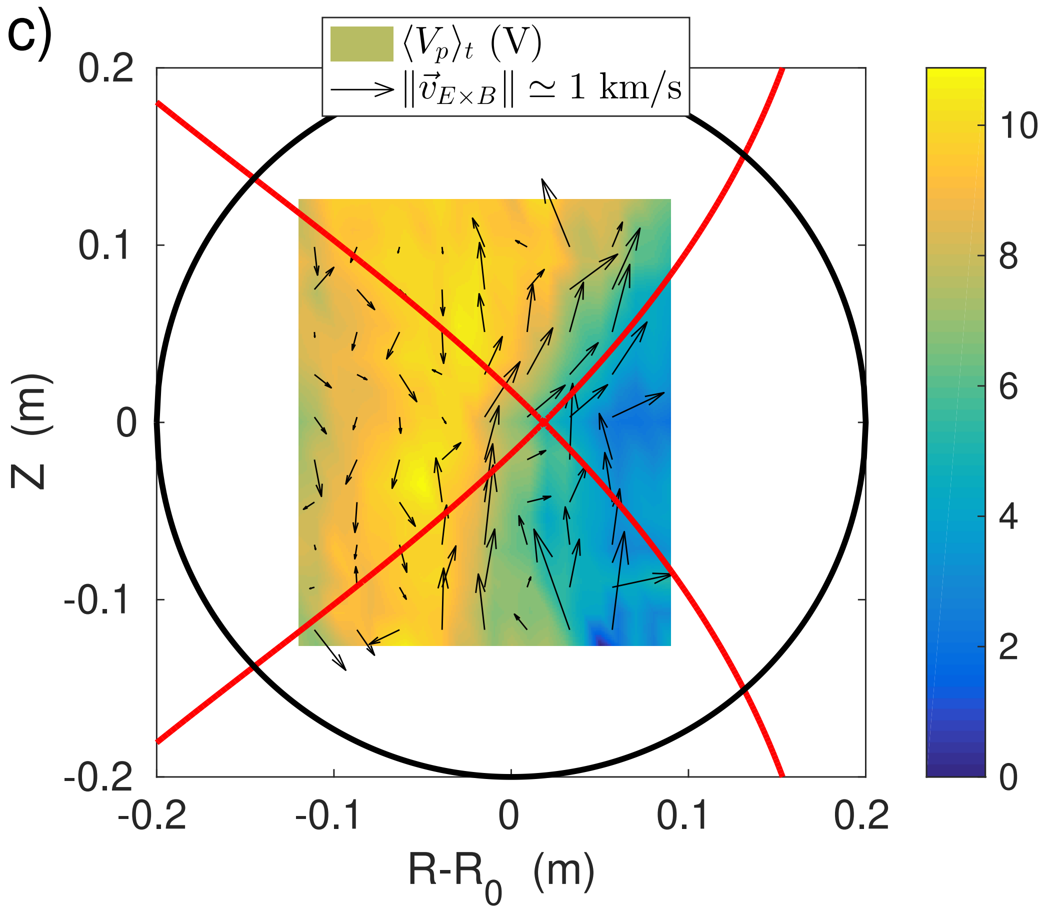
c)
$\langle V_p\rangle_t$ (V)
$\longrightarrow \|\vec{v}_{E\times B}\| \simeq 1$ km/s
0.2
0.1
0
-0.1
-0.2
Z (m)
-0.2
-0.1
0
0.1
0.2
R-R_0 (m)
10
8
6
4
2
0

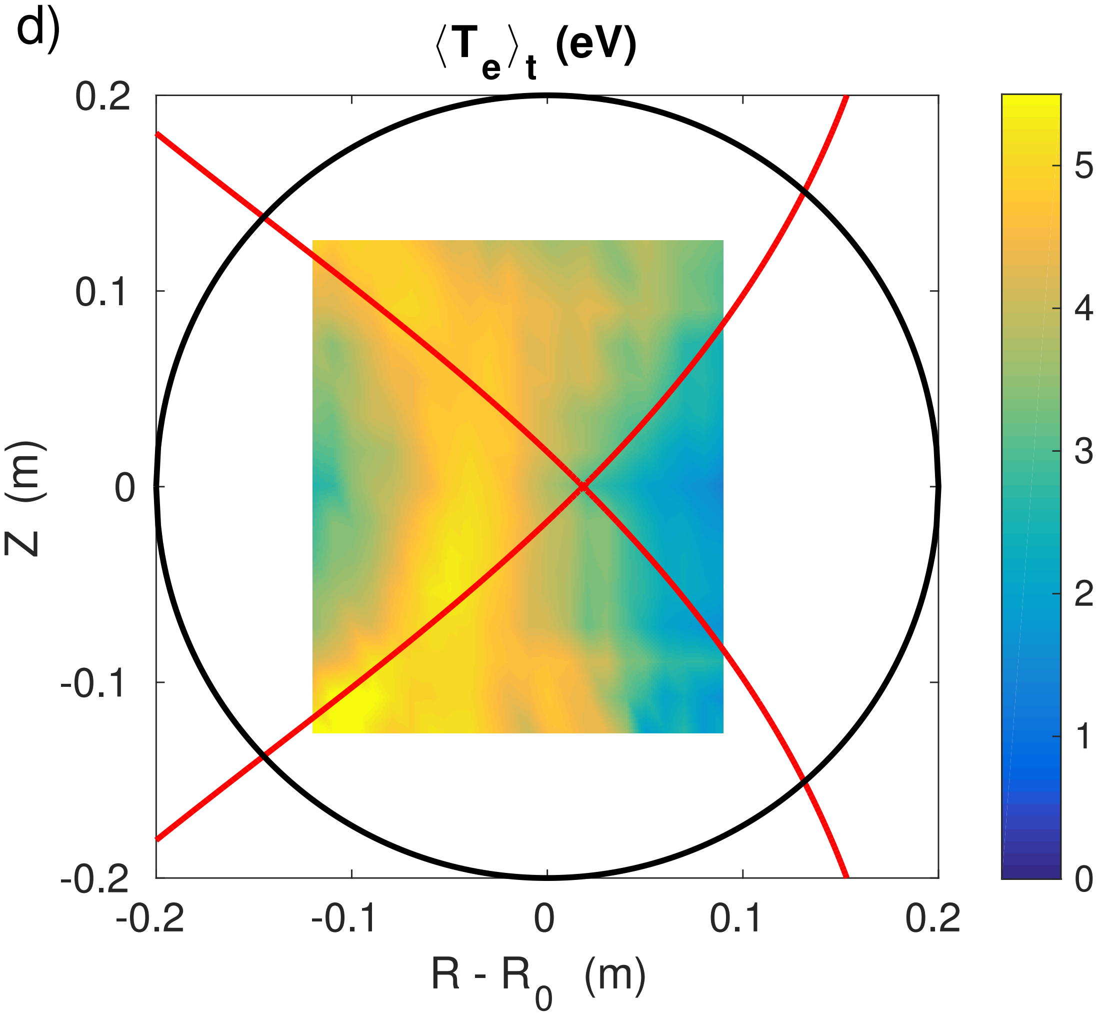
d)
⟨T_e⟩_t (eV)
0.2
0.1
0
-0.1
-0.2
Z (m)
-0.2
-0.1
0
0.1
0.2
R - R_0 (m)
5
4
3
2
1
0

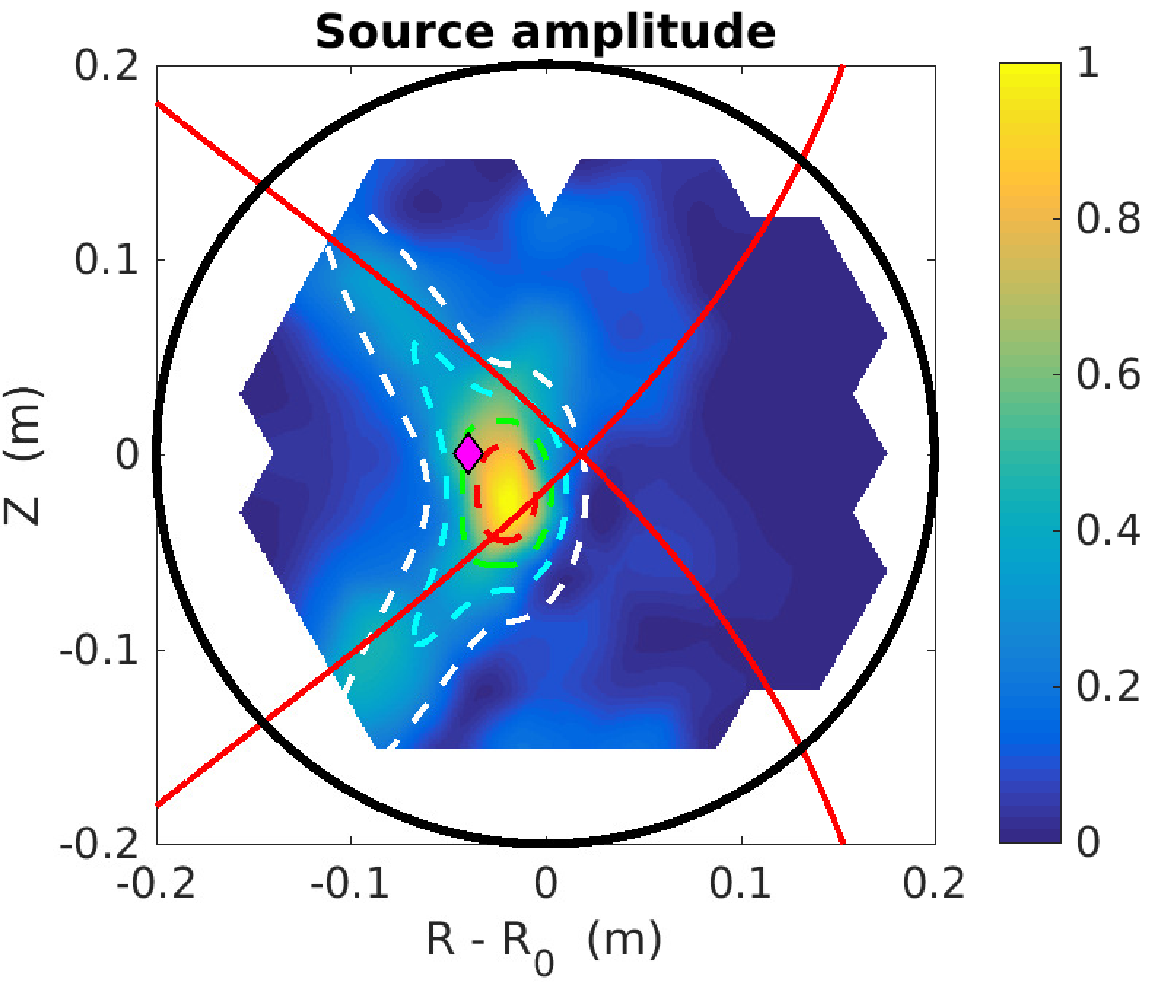
Source amplitude
0.2
0.1
0
-0.1
-0.2
Z (m)
-0.2
-0.1
0
0.1
0.2
R - R_0 (m)
1
0.8
0.6
0.4
0.2
0

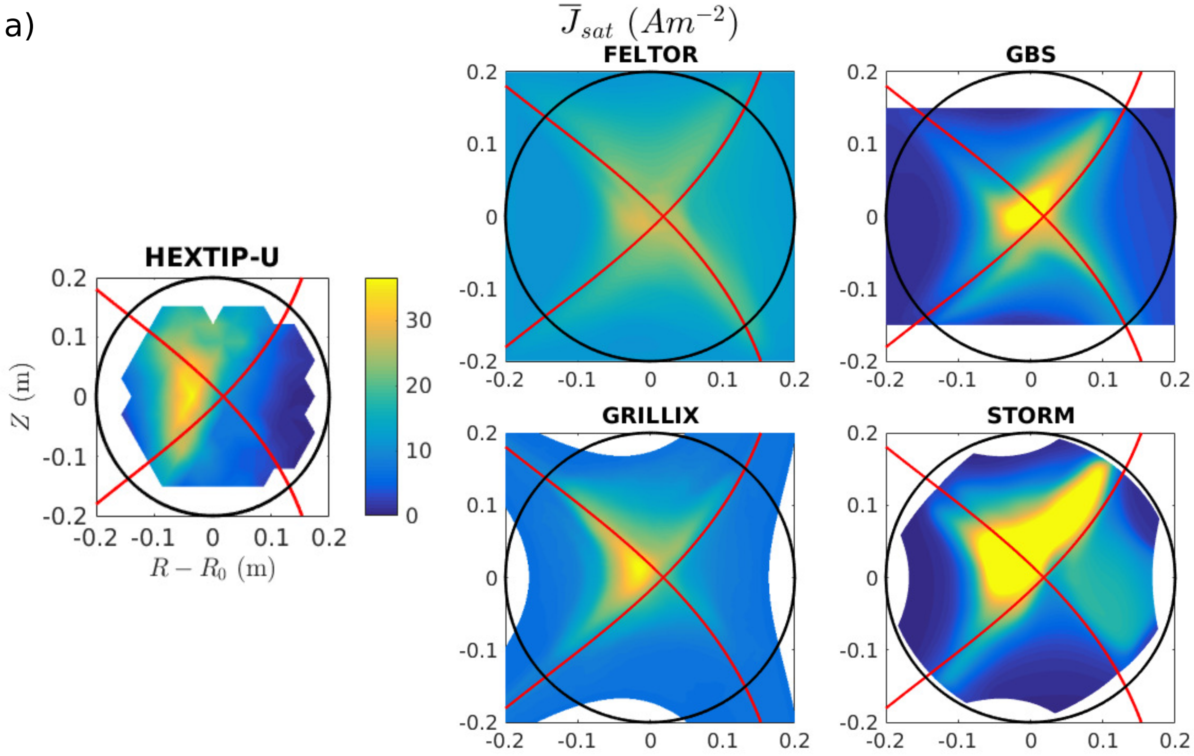
a)
$\overline{J}_{sat}\ (Am^{-2})$
HEXTIP-U
FELTOR
GBS
GRILLIX
STORM
Z (m)
$R - R_0$ (m)
0.2
0.1
0
-0.1
-0.2
30
20
10
0

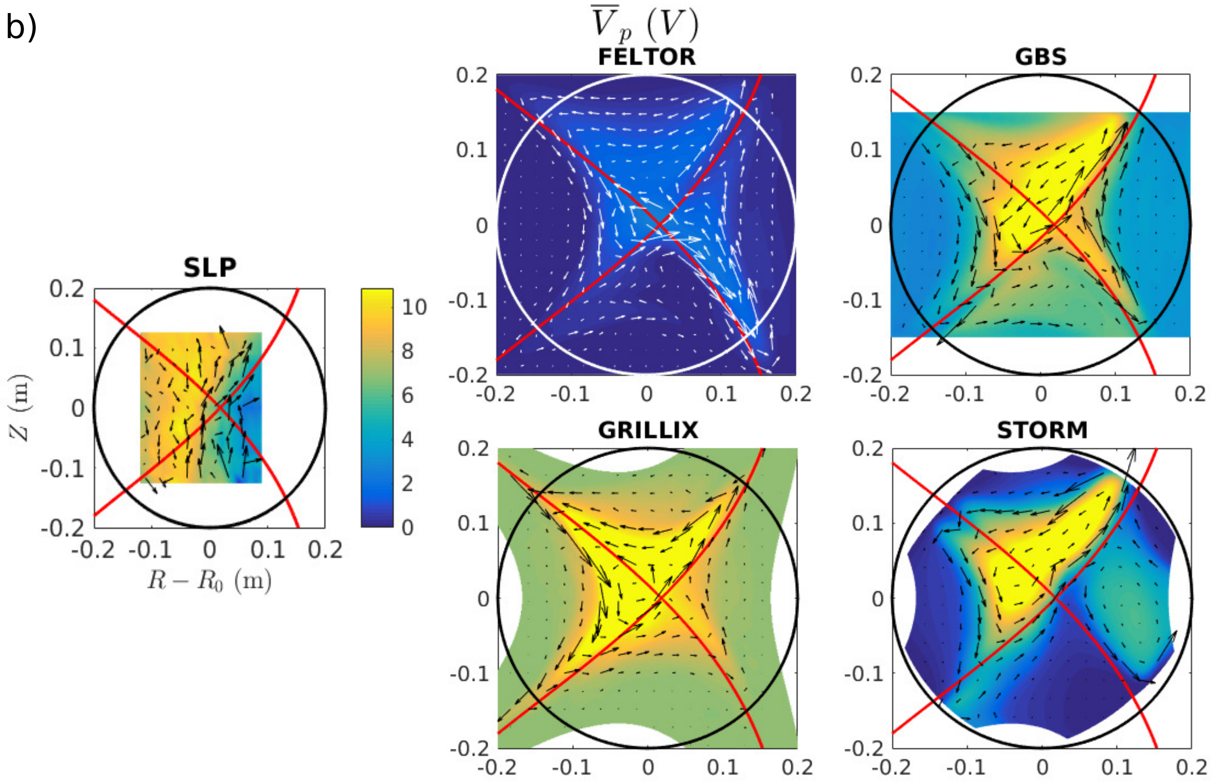
b)
$\overline{V}_p\ (V)$
FELTOR
GBS
SLP
GRILLIX
STORM
Z (m)
$R - R_0$ (m)
0.2
0.1
0
-0.1
-0.2
-0.2
-0.1
0
0.1
0.2
10
8
6
4
2
0

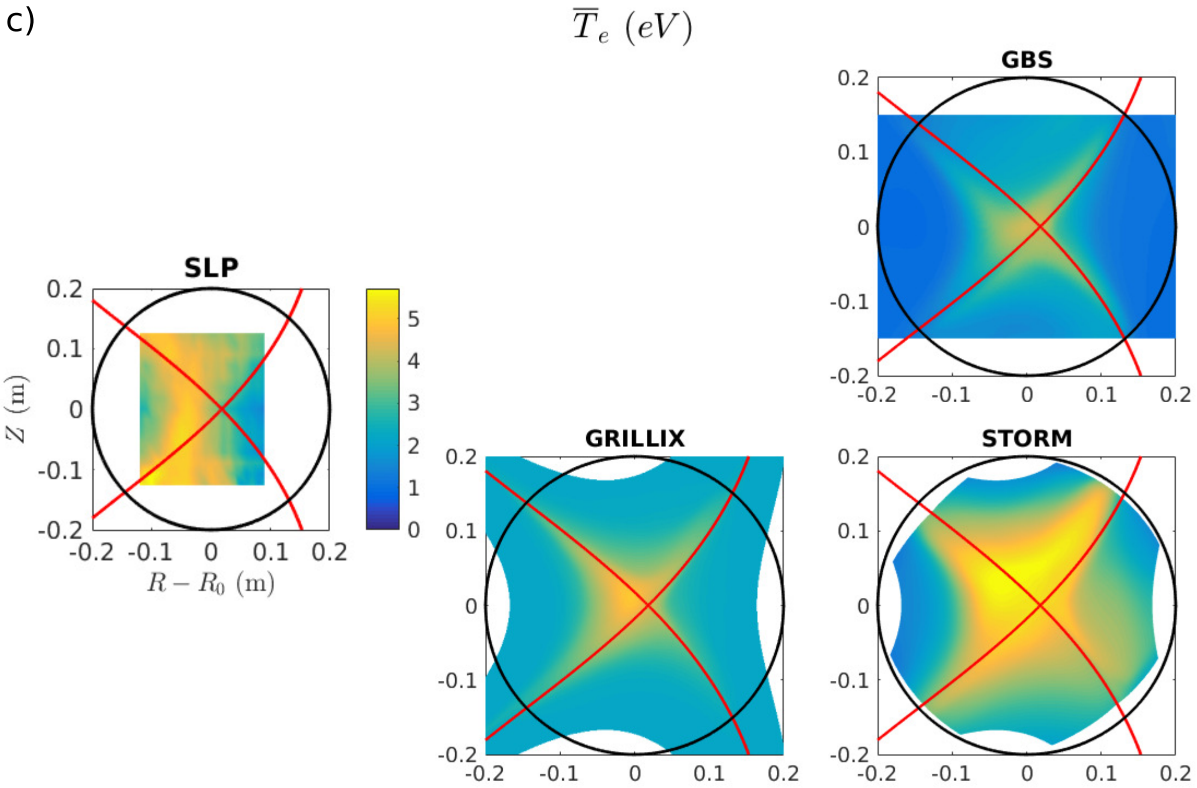
c)
$\overline{T}_e\ (eV)$
SLP
GBS
GRILLIX
STORM
Z (m)
$R - R_0$ (m)
0.2
0.1
0
-0.1
-0.2
5
4
3
2
1
0

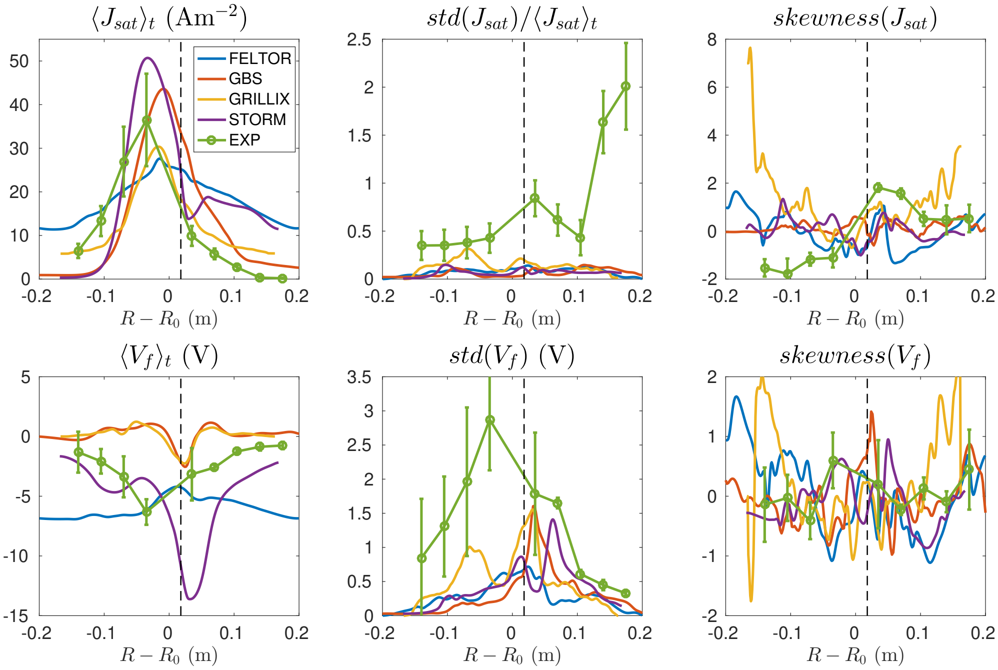
$\langle J_{sat}\rangle_t$ (Am^{-2})
$std(J_{sat})/\langle J_{sat}\rangle_t$
$skewness(J_{sat})$
FELTOR
GBS
GRILLIX
STORM
EXP
$\langle V_f\rangle_t$ (V)
$std(V_f)$ (V)
$skewness(V_f)$
$R-R_0$ (m)
-0.2
-0.1
0
0.1
0.2
50
40
30
20
10
2.5
2
1.5
1
0.5
8
6
4
-2
5
-5
-10
-15
3.5
3

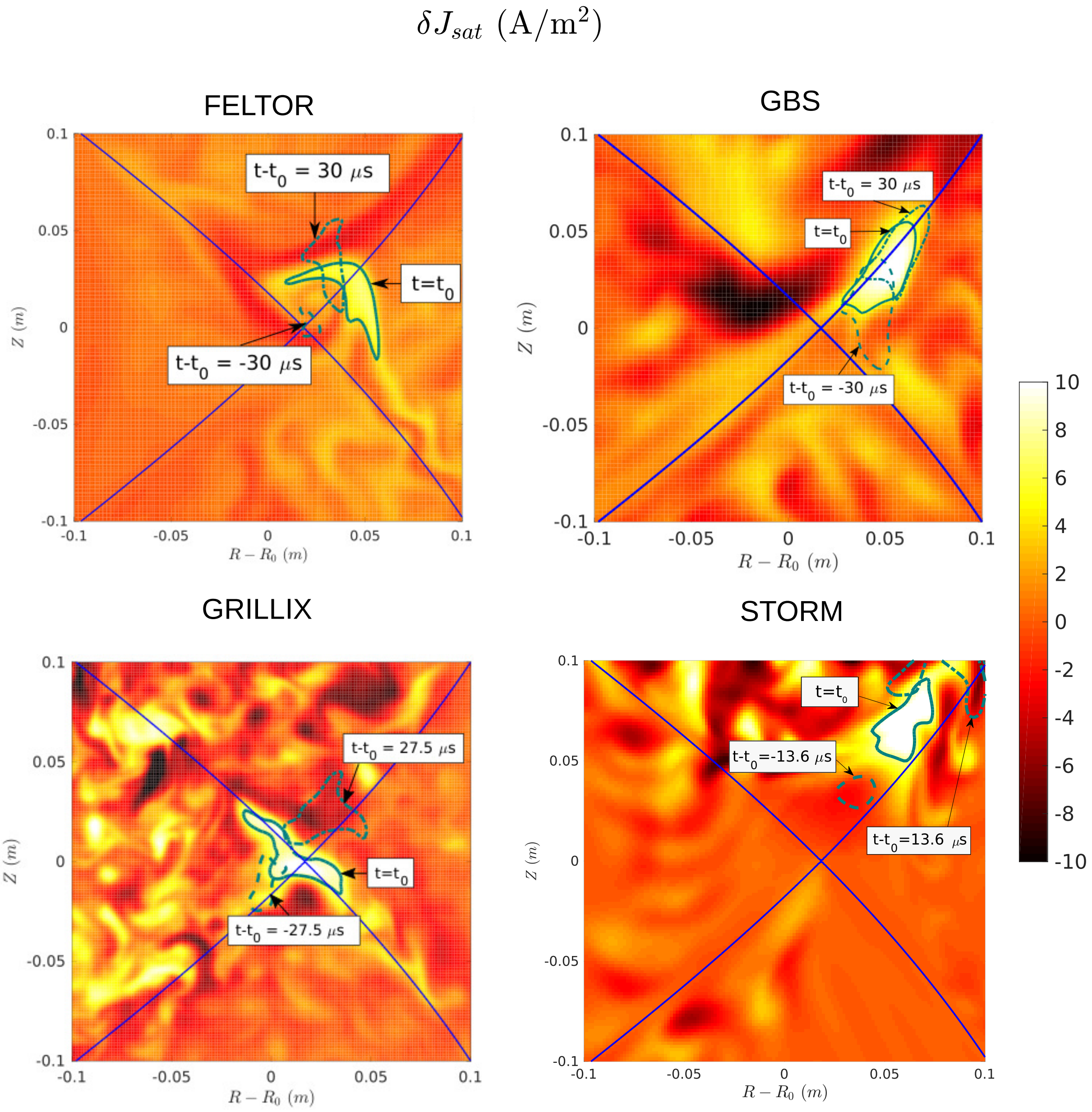
δJ_{sat} (A/m^2)
FELTOR
GBS
GRILLIX
STORM
t-t$_0$ = 30 μs
t=t$_0$
t-t$_0$ = -30 μs
t-t$_0$ = 27.5 μs
t-t$_0$ = -27.5 μs
t-t$_0$=-13.6 μs
t-t$_0$=13.6 μs
Z (m)
$R - R_0$ (m)
0.1
0.05
0
-0.05
-0.1
10
8
6
4
2
0
-2
-4
-6
-8
-10

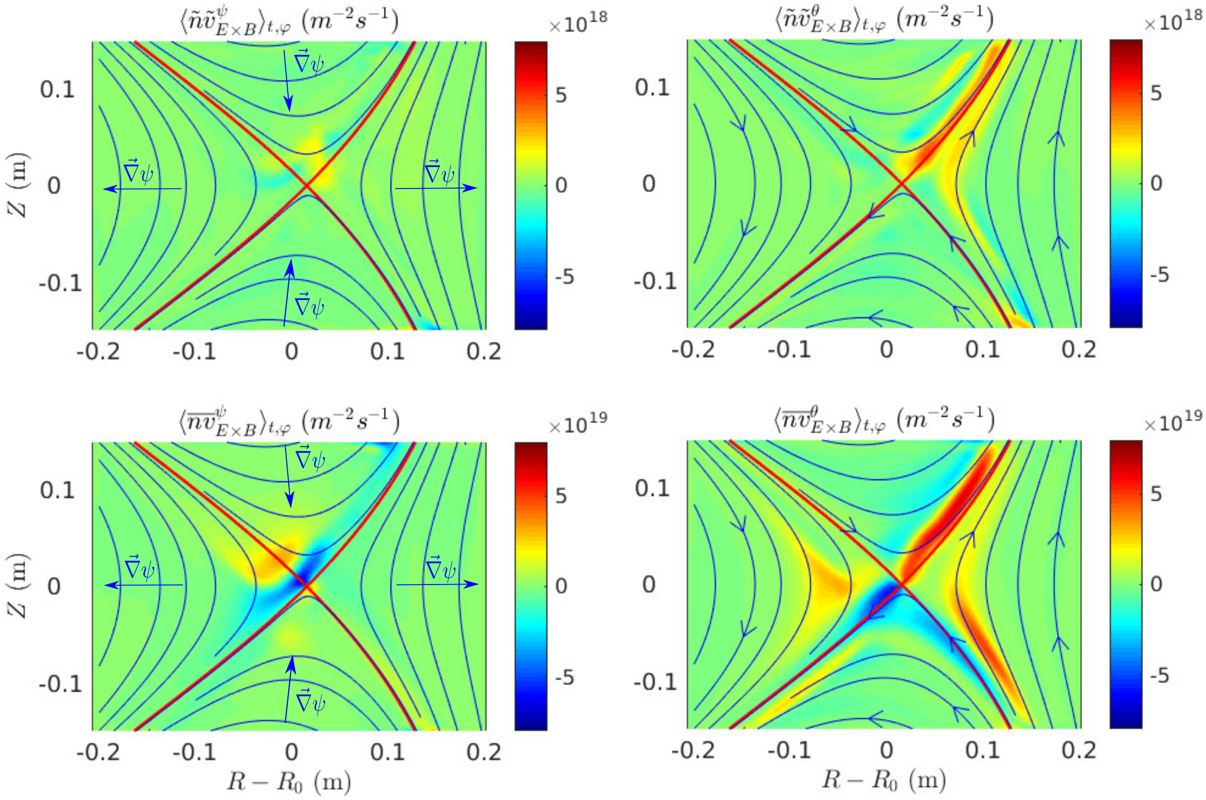
$\langle \tilde{n}\tilde{v}^{\psi}_{E\times B}\rangle_{t,\varphi}$ $(m^{-2}s^{-1})$
$\times 10^{18}$
$\langle \tilde{n}\tilde{v}^{\theta}_{E\times B}\rangle_{t,\varphi}$ $(m^{-2}s^{-1})$
$\times 10^{18}$
$\langle \overline{n}\overline{v}^{\psi}_{E\times B}\rangle_{t,\varphi}$ $(m^{-2}s^{-1})$
$\times 10^{19}$
$\langle \overline{n}\overline{v}^{\theta}_{E\times B}\rangle_{t,\varphi}$ $(m^{-2}s^{-1})$
$\times 10^{19}$
$\vec{\nabla}\psi$
Z (m)
$R - R_0$ (m)
0.1
0
-0.1
-0.2
0.2
5
-5

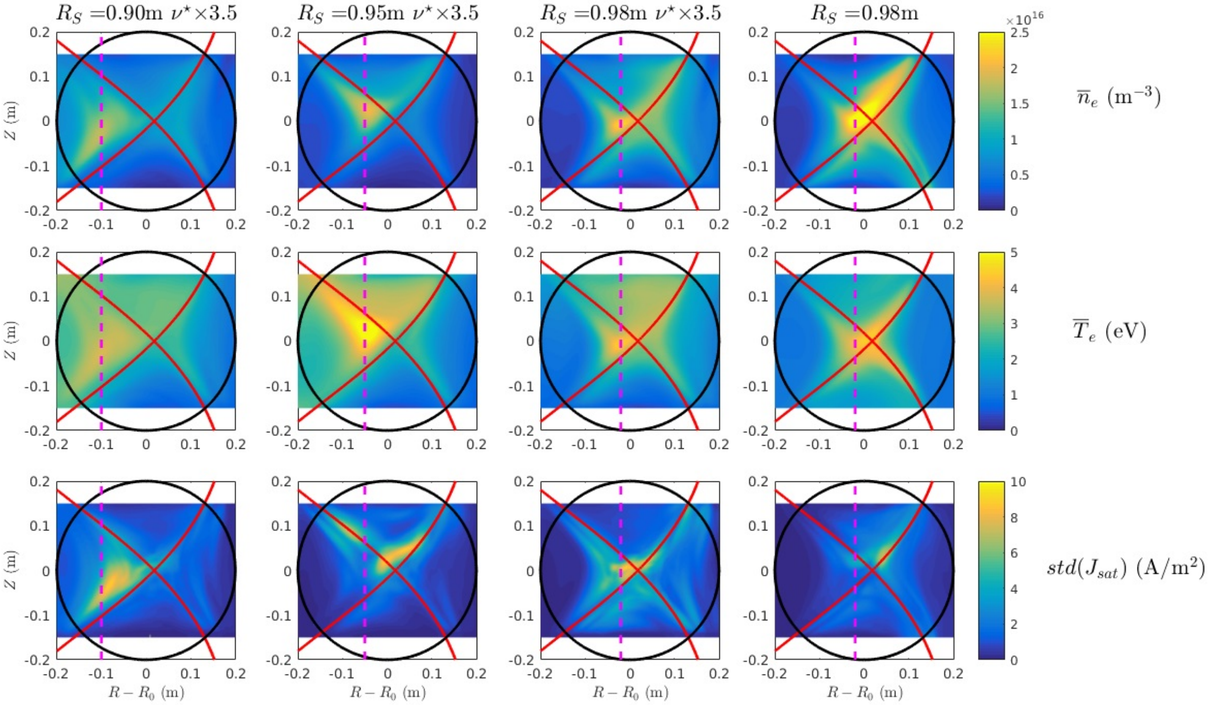
R_S =0.90m $\nu^\star\times$3.5
R_S =0.95m $\nu^\star\times$3.5
R_S =0.98m $\nu^\star\times$3.5
R_S =0.98m
Z (m)
$R-R_0$ (m)
-0.2
-0.1
0
0.1
0.2
$\times10^{16}$
2.5
2
1.5
1
0.5
0
$\overline{n}_e$ (m^{-3})
5
4
3
2
1
0
$\overline{T}_e$ (eV)
10
8
6
4
2
0
$std(J_{sat})$ (A/m^2)

the most direct measurements, and thus also the most important to be matched by simulations. The quality of the comparison is then calculated as:

$$Q = \sum_j H_j S_j \ , \tag{4.5}$$

and it is a measure of how stringent or extensive the validation is [22], increasing with the number of observables and with their precision, and decreasing with their hierarchy level. The overall level of agreement between a simulation and the experiment, or "metric", is defined as:

$$\chi = \frac{\sum_j R_j H_j S_j}{\sum_j H_j S_j} \ , \tag{4.6}$$

where $\chi \in [0;1]$, $\chi = 0$ indicating perfect agreement and $\chi = 1$ no agreement. When applying the validation procedure to FELTOR, which is isothermal, electron temperature is excluded from the list of observables. The time-averaged floating potential is also excluded, since it is calculated as $V_f = \phi - \Lambda T_e$, so through a model of the sheath dependent on T_e, which is not applicable to FELTOR simulations. Moreover, for FELTOR we calculate the statistical moments of the plasma potential ϕ instead of the floating potential V_f, since in an isothermal model these fields differ only by a constant. The results of the validation procedure for each code are reported Table 4.

	FELTOR	GBS	GRILLIX	STORM	GBS $\nu^\star \times 3.5$ R_S=0.90m	GBS $\nu^\star \times 3.5$ R_S=0.95m	GBS $\nu^\star \times 3.5$ R_S =0.98m
$\overline{J}_{sat}$	46.5	14.5	20.6	17.85	26.7	11.3	19.9
$std(J_{sat})/\overline{J}_{sat}$	6.76	2.77	2.73	2.68	3.00	2.84	2.14
$skewness(J_{sat})$	3.91	4.27	9.42	4.93	23.3	21.1	4.72
$\overline{V}_f$		8.39	6.77	8.58	7.33	9.65	14.9
$std(V_f)$	70.9	5.76	6.11	5.22	8.06	7.40	6.40
$skewness(V_f)$	3.27	2.50	8.69	2.75	22.2	18.8	2.35
$\overline{V}_p$	3.06	1.28	1.33	1.60	1.26	2.35	1.62
$\overline{n}_e$	5.02	3.85	1.72	4.75	2.67	1.86	2.68
$\overline{T}_e$		4.02	2.63	2.35	2.75	1.72	3.38
Q	2.86	3.50	3.63	3.54	3.72	3.74	3.58
χ	1.00	0.89	0.85	0.93	0.90	0.93	0.93

Table 4: Distance d_j evaluated for all the observables in all the simulations. A green color indicates a good agreement, while the more the background color tends to the red, the larger the disagreement. The colorscale is saturated at 5, and empty fields correspond to quantities not simulated by the code. The last two lines indicate the quality Q and the metric χ for each simulation. The last three columns are referred to the simulations discussed in Section 5.

Globally, the agreement between numerical and experimental results, identified by the metric χ, is not satisfactory from a quantitative point of view, as visible in Table 4. We remark here, however, that not considering numerical errorbars makes this comparison particularly strict with respect to previous validation works (e.g. [23, 25]). FELTOR, GBS, GRILLIX and STORM simulations result in a level of agreement of $\chi \simeq 1.00, 0.89, 0.85$ and 0.95, respectively. The observables determining these